

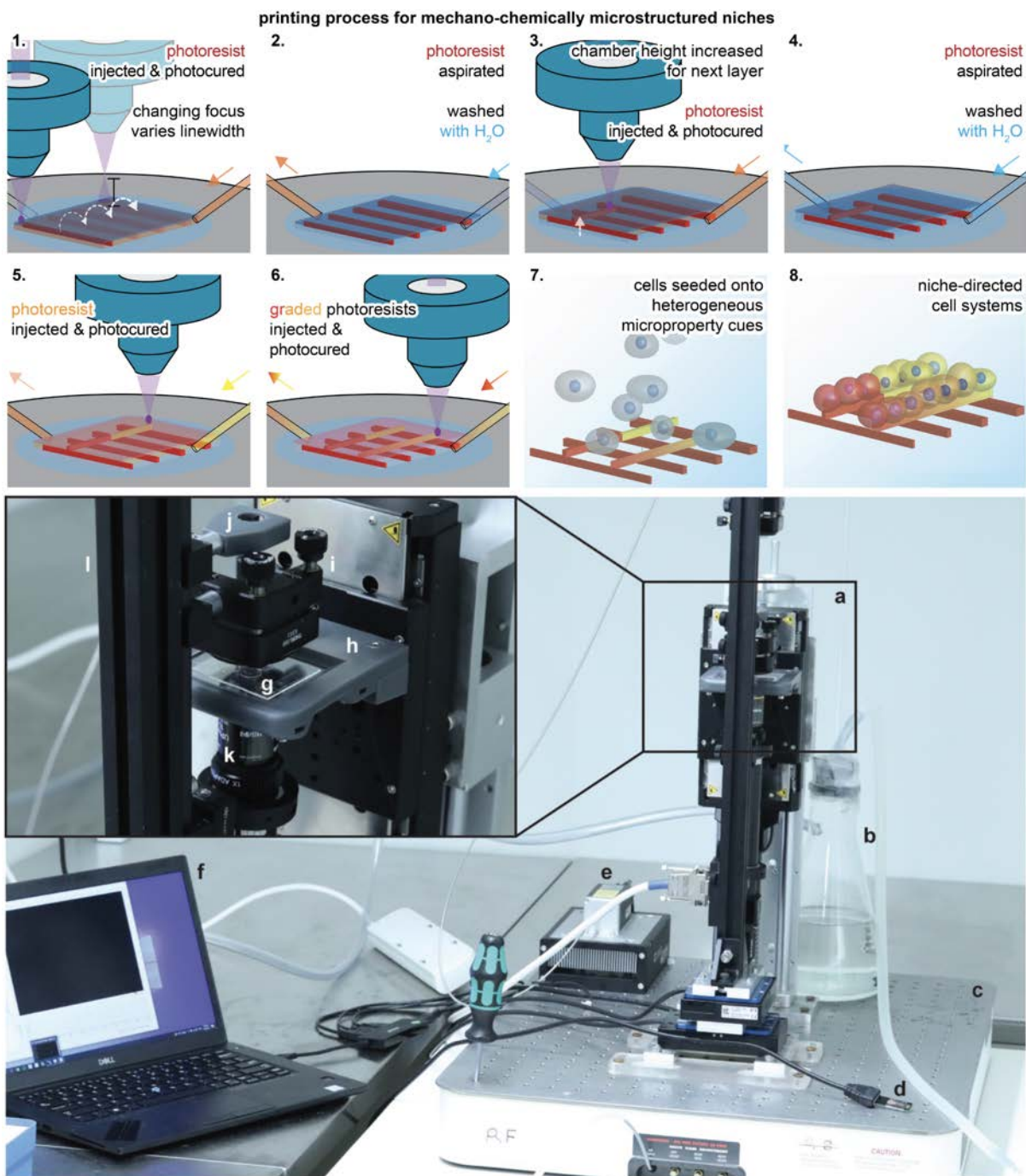
## Supplementary materials for

# Programming of multicellular patterning with mechano-chemically microstructured cell niches

- 5   **Prior literature on printing, and a comparison of printing approaches.** One promising technology to generate complex niche environments is printing. Standard printing methods involve the extrusion of a biopolymer ink or the direct extrusion of cells. Extrusion printers can produce materials with discrete properties through the sequential extrusion of different materials, either from separate print cartridges, each loaded with different bioinks<sup>[1-5]</sup>, or
- 10   through mixing solutions before their extrusion through a single nozzle<sup>[6,7]</sup>. Demonstrated structured properties include changes to embedded cell types<sup>[4,8]</sup>, mechanical properties<sup>[3,7]</sup>, and biochemicals<sup>[9]</sup>. Structured materials are analogous to a pixelated digital image, where finite-area elements of specific local properties – e.g., in the case of an image: specific colors – are combined to achieve an emergent function. While the pixel organization of digital
- 15   images reconstructs visual information, printed multi-or-structured materials can function as a device. Structured materials fabricated with extrusion printing are limited in the number of different material types by the number of print cartridges or their ability to efficiently switch and mix solutions within a single print cartridge. Accordingly, structured cell systems fabricated from extrusion printing have been limited to no more than three cell inks<sup>[5,10]</sup>, and
- 20   have not been demonstrated with comparable feature sizes to those possible through alternative printing methods, including photolithography<sup>[11]</sup>. These limitations make the extrusion approach problematic for fabricating biomaterials with microstructured properties. As an alternative approach to indirectly structuring tissues with environmental cues, organoid models have been generated using direct extrusion printing of hiPSCs<sup>[8,12,13]</sup>. hiPSCs can be
- 25   directly extruded into defined architectures and subsequently differentiated on the provision of external media-derived cues or intercellular feedback from concurrently extruded differentiated cells. While this approach permits the generating macroscale organoids with improved reproducibility, these models still rely on self-organizing processes, limiting their size and tissue complexity constraining the acquisition of higher-level cellular functions.
- 30   Photolithography is an alternative 3D printing method that uses light to selectively polymerize a material from a photoresist. This method offers technical solutions to some obstacles faced when extrusion-printing complex materials. For example, photolithographic

printing methods have generated materials with nanoscale features<sup>[14]</sup>, a feat yet to be achieved using extrusion-printing. Early work developing heterogeneous biomaterials with  
35 chemically discrete properties used photolithography to pattern regions of small bioactive molecules and peptides<sup>[15–17]</sup>, with more recent methods capable of the spatiotemporal micro-structuring complex biomacromolecules<sup>[18]</sup>, and discrete mechanical microproperties<sup>[19]</sup>.

40 **Overview of the custom built printer.** Details of the custom-built mechano-chemical flow lithographic (MCFL) printer, including a schematic overview of it's operation, and it's parts are provided below including the printing method in-line explanatory figures (**Figure S1**). This includes fabricating one-time-use glass components, calibrating the printer, loading photoresists, printing, software use, and preparing samples for cell seeding. All components of the printer are detailed in **Table S 1**.



45

**Figure S1. Overview of printing process and photography showing the labeled setup of the MCFL printer.** A schematic showing the stepwise fabrication processes to print synthetic cell niche environments is labelled and shown at the top of the figure. **a**, MCFL printer stage. **b**, vacuum system. **c**, optical breadboard table. **d**, LED touch light. **e**, diode laser and heatsink. **f**, computer with software. The inset at the top left shows a detailed view of the print chamber. **g**, glass sample chamber. **h**, custom-printed stage. **i**, mounted aspheric lens. **j**, optical rail. **k**, custom-printed LED housing. **l**, objective lens.

50

Niches were fabricated on glass 10 mm diameter size #1 coverslips by the injection or 'flowing' of photoresists of variable biochemical and polymeric composition through a print

chamber during printing (**Figure. 1**, **Figure. S1h**, see **Table S 2** for specific photoresist compositions). **Figure S2** shows an isolated view of the printer stage platform, alongside the PDMS coated glass slide loaded with four coverslips.

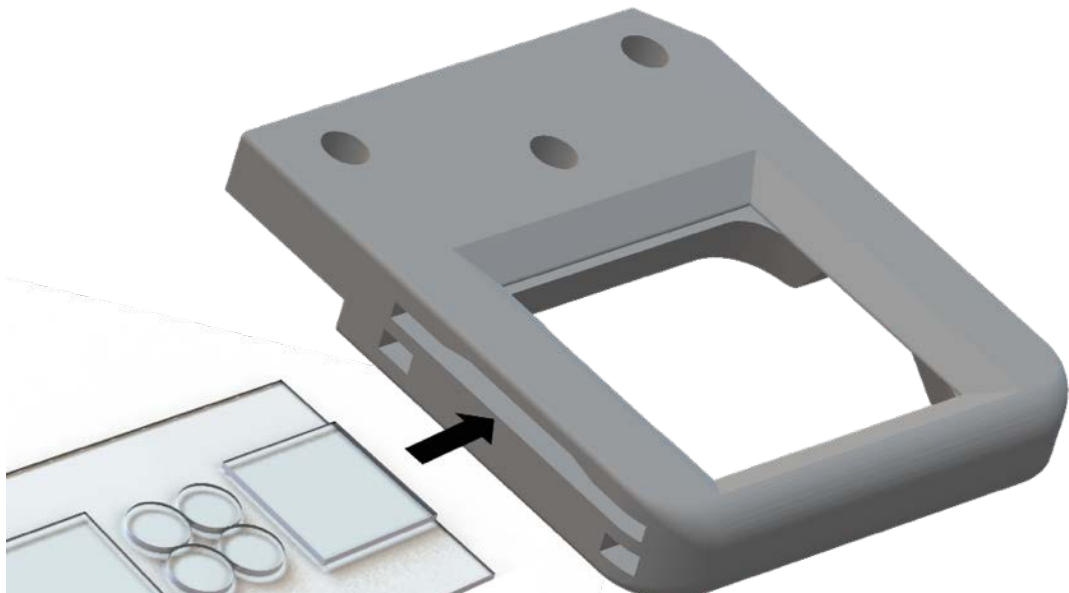


**Figure S2. Schematic of custom-printed stage housing for printing chamber.** The constructed printing chamber base is inserted into the side slot and secured through clamping bolts under each corner. A photoresist is injected onto the 10 mm acrylated coverslips, and a PDMS-coated top slide is positioned centrally over the opening.

**Fabrication of print chamber and sample coverslips.** A photoresist is injected onto 10 mm diameters coverslips sandwiched by two hydrophobic PDMS coated glass slides during printing. This forms the print chamber (**Figure S1-a,b**), is then clamped into the printer stage. PDMS coated 50x75x1 mm glass slides (Sigma CLS294775X50) are prepared using PDMS (Corning Sylgard 184) ten-parts base to one-part curing agent. The solution is mixed with a metal spatula and briefly centrifuged to remove bubbles. Glass slides are spin-coated with PDMS on a Laurell EDC 650 series spin coater. PDMS is poured onto the top of the samples at approximately an Australian 50 cent piece volume. The spin coater is then ramped to 1600 rpm for 10 s and stopped. The glass slides are then placed onto a hot plate at 200 °C for 1 min before being transferred to a 37 °C oven overnight.

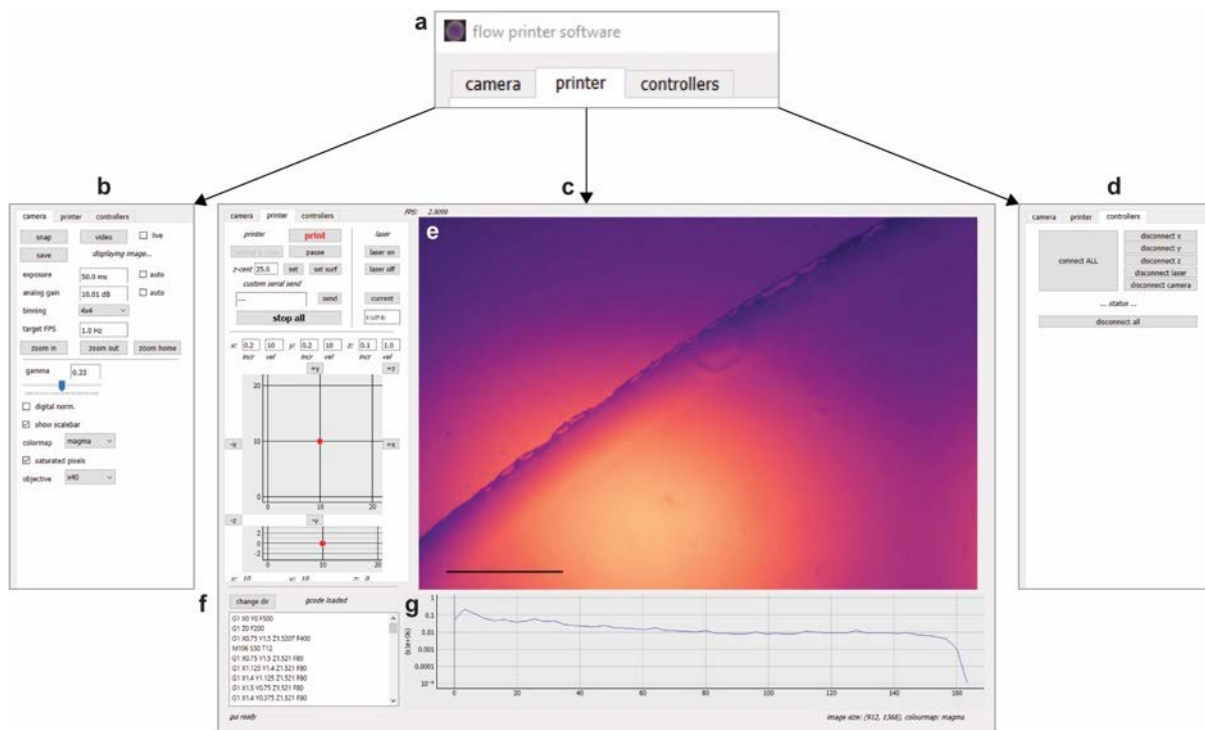
Printing was completed on an acrylate-functionalized coverslip base that forms a stable substrate for transport and culture of the printed materials, including the prevention of sample delamination, sample-folding, or strain deformation due to hydrogel swelling, as well, the covalent attachment assists sample handling for downstream cell culture. A silanization

75 solution was prepared to functionalize coverslips. A glass dish was washed with methanol  
(Sigma 322415) by bath sonicating for 5 minutes in a chemical safety fume hood. The dish  
was then dried then rinsed a further x2 with methanol. 100 mL of methanol, 5 mL of glacial  
acetic acid (Sigma A6283), and 3 mL 3-(trimethoxy silyl) propyl acrylate (TCI A1597) was  
added to the dish along. Circular glass coverslips were washed x3 times in methanol before  
80 being placed in the silanization solution. The dish was covered to prevent evaporation or  
contamination from ambient H<sub>2</sub>O. Coverslips are left for one hour for the silanization  
reaction to proceed. Coverslips were then rinsed x3 in ethanol, wiped clean, and dried with  
N<sub>2</sub>. All glass and PDMS components are thoroughly washed with warm tap water, Triton X-  
100, acetone, isopropanol, and purified water once again prior to printing. The glass is then  
85 air-dried using high-pressure filtered compressed air to limit dust particles and lint on  
samples.

The print chamber is assembled by suctioning the acrylated coverslips onto the PDMS-coated  
glass slide. A single print may consist of four 10 mm coverslips positioned in the middle of  
the slide (**Figure S2**). Suction force holds sample coverslips to the PDMS coating. Plain  
90 square glass coverslips (24 mm x 24 mm) are positioned adjacent to each short edge of the  
PDMS slide to ensure the correct elevation of the chamber's top (**Figure S2**). The top  
chamber uses an opposing PDMS glass slide and effectively sandwiches the acrylated  
substrate coverslips within a hydrophobic glass chamber when positioned on top. The printer  
setup is housed within a dark 4°C cold room pictured throughout - to limit photoactivation of  
95 the resist, as well as damage, misfolding, and gelling of sensitive biochemical reagents. All  
printer components and reagents are stored in the cold room to acclimatize before printing,  
preventing condensation. The base PDMS slide is inserted into the printing stage and secured  
into position through bolts at the bottom of each corner (**Figure S2**). The chamber's top is  
then positioned to calibrate coverslips and chamber height. Machine bolts then attach the  
100 printer stage to the rest of the printer.

**Calibration of printer laser with sample coverslips and stage.** A camera assembly is  
mounted below the printing stage to monitor laser alignment and focus. The printer's laser is  
first calibrated to the camera assembly (**Table S 1** for component details) using the custom  
105 printer software (**Figure S3**). The distance between the laser and camera assembly is altered  
for parfocality. The camera is focused on the stage by changing the stage height. The laser is

then focused through a position that passes the acrylated coverslip by navigation using the GUI stage map within the printer control panel (**Figure S3c**). Focusing the laser at this position ensures an accurate focal length of the light path that includes the refractive differences of all materials and prevents aberrations caused by coverslip edges. During this step, focal asymmetry and astigmatisms can be reduced by carefully calibrating machine thumbscrews on mechano-optical components housing the laser fiber unit, collimator, beam expander, and focal objective (for parts numbers see **Table S 1**).



115 **Figure S3. Labelled layout of software for printer operation.** Three panels are available to control printer parameters; camera, printer, controllers. **a**, Software interface panels. **b**, camera control. **c**, printer control. **d**, printer connection diagnostics with controllers. **e,g** live camera image output (pictured at the calibrated edge of coverslip sample). **f**, gcode input/output, and control. Standalone printer software as written in python with PyQt5 is available for download from supplemental information.

120 The stage height is adjusted to focus on the print sample during laser calibration, ensuring calibration between the laser, camera, and stage/samples. Camera parameters such as exposure, gain, binning, frames per second (FPS), and gamma may be adjusted in the GUI to visualize the live image better. A further feature of the camera view includes toggles for colormap, scalebar, digital normalization, saturated pixels, and objective may also be toggled for viewing experience (**Figure S3b**).

**Injection of photoresist into glass print chamber.** Following calibration of the printer, a photoresist is injected within the print chamber onto the acrylated coverslips. Accurate assembly of the print chamber results in a 50 µm void between the PDMS top slide and sample for photoresist injection.

130

**gcode upload and print initiation.** The software interprets and translates gcode commands, sending these to the PI controllers - (V-528.1AA /V-528.1AB and M-406 including corresponding controllers C-413 and C863 from Physik Instrumente (PI) GmbH & Co. KG). The gcode is loaded by navigating to the relevant directory and then visually verified through 135 the log on the bottom left of the GUI (**Figure S3f**). An inspection of the printing area is performed to ensure no objects are obstructing printer movement. Printing is initiated and confirmed for correct laser movement. If errors are present, printing may be paused or terminated in the GUI. When performing a print with multiple photoresists, the vacuum pump is used to suction any excess photoresist from the previous print. The coverslips are gently 140 washed with PBS supplemented with penicillin and streptomycin. If a printer connection is lost during the process, this may be troubleshooted using the controller tab. Here, the connection to the stage, laser, and camera may be disconnected or reconnected. Otherwise, the printer may be switched on and off to restore the connection.

145 **Removal of samples from the printer.** The top slide is carefully removed after printer termination to ensure that the printed substrate is not damaged or attached to the chamber. The stage is then unfastened from the printer and removed. The printer chamber is unclamped and taken out of the stage, revealing the samples. For each coverslip, a well of a 48-well plate is prepared with 0.5 mL of PBS supplemented with penicillin and streptomycin. Coverslips 150 are removed from the base PDMS-coated glass using a scalpel blade to gently disturb the suction forces between the sample base and the PDMS. Care is taken not to damage the printed substrate or glass coverslip. The coverslips are then moved to a well, ensuring that the printed substrate faces the right side upwards. Well plates containing samples should then be parafilmed and left to wash on a plate rocker at 4 °C for 48h before use. Samples have been 155 stored for up to 1 week without observing any changes to their function.

**Sterilization and preparation of printed substrates.** The printed niches are washed two times with sterile PBS prior to cell seeding. While submerged, samples are UV-sterilized in a biosafety cabinet for 12 minutes, with the plate lid removed. For circular glass control samples, coverslip samples are incubated with hESC qualified Matrigel® (Corning) for 1 hour before cell seeding.

**3D structures in Figure 1.** The printed structures presented in **Figure 1h,i** were achieved as per Grigoryan et al.<sup>[20]</sup>, adding 3 mM of the photoabsorber tartrazine, as to limited the penetration depth of the laser . A full optimization of the variable state-space for MCFL of 3D structures using the tartrazine methods was unexplored in the present study. As per discussions points, this approach may permit further exploration of the method using complex 3D structures.

**Software, installation, and use.** github code and supporting materials can be found [this repository](#) - [github.com/peterlionelnewman/flow\\_lithographic\\_printer](https://github.com/peterlionelnewman/flow_lithographic_printer). Where further supportive installation and use instructions can be found. This software has been written for use with the controllers and hardware listed in Table S1 at bottom. Where possible all code has been provided, some of the SDK and python packages are licensed and supplied by component manufacturers.

**Table S 1. Printer parts and components.** Labels column references item locations are annotated over **Figure S1**.

| Category    | Description   | Label |
|-------------|---|-------|
| Laser Mount | <a href="#">RC4 - Dovetail Rail Carrier, 0.60" x 1.00" (15.2 mm x 25.4 mm), #8 (M4) Counterbore</a> |       |
|             | <a href="#">K5X1 - 5-Axis Locking Kinematic Mount for Ø1" Optics</a>                                |       |
| Laser 2     | <a href="#">Cobolt 06-01 Series 405 nm, fiber pigtailed, FC/APC</a>                                 | S1e   |
|             | <a href="#">HS-03 Heat Sink</a>   |       |
|             | <a href="#">405 nm FC/APC Collimation Package, NA = 0.26, f = 33.9</a>                              |       |
|             | <a href="#">K5X1 - 5-Axis Locking Kinematic Mount for Ø1" Optics</a>                                |       |

|                     |   |             |
|---------------------|---|-------------|
|                     | <a href="#">RC4 - Dovetail Rail Carrier, 0.60" x 1.00" (15.2 mm x 25.4 mm), #8 (M4) Counterbore</a>   |             |
| Aspheric Lens       | <a href="#">RC4 - Dovetail Rail Carrier, 0.60" x 1.00" (15.2 mm x 25.4 mm), #8 (M4) Counterbore</a>   | S1a,<br>S1i |
|                     | <a href="#">KM100T - SM1-Threaded Kinematic Mount for Thin Ø1" Optics</a>                             |             |
|                     | <a href="#">S1TM12 - SM1 to M12 x 0.5 Lens Cell Adapter</a>   |             |
|                     | <a href="#">A240TM - f = 8.0 mm, NA = 0.50, Mounted Rochester Aspheric Lens, Uncoated</a>             |             |
| Optic Rail          | <a href="#">XE25L900/M - 25 mm Square Construction Rail, 900 mm Long, M6 Taps</a>                     | S11         |
|                     | <a href="#">RLA300/M - Dovetail Optical Rail, 300 mm, Metric</a>                                      |             |
|                     | <a href="#">RLA300/M - Dovetail Optical Rail, 300 mm, Metric</a>                                      |             |
|                     | <a href="#">XE25L225/M - 25 mm Square Construction Rail, 225 mm Long, M6 Taps</a>                     |             |
| Sample/Slide Holder | <a href="#">KM100C - Kinematic Mount for up to 1.3" (33 mm) Tall Rectangular Optics, Right Handed</a> | S1h, S2     |
|                     | <a href="#">Manual XYZ trimming stage for placing transparent stage</a>                               |             |
|                     | Z stage with sample holder Figure S1,2  |             |
| Stage 3 10nm        | <a href="#">M-406.2DG Precision Linear Stage</a>  | S1          |
|                     | <a href="#">V-528.1AA High-Dynamics PIMag® Linear Stage</a>   |             |
|                     | <a href="#">V-528.1AB High-Dynamics PIMag® Linear Stage</a>   |             |
|                     | <a href="#">C-413.2G PIMag® Motion Controller</a>   |             |
|                     | <a href="#">C-863 Mercury Servo Controller</a>  |             |
| Camera Assembly     | <a href="#">RC4 - Dovetail Rail Carrier, 0.60" x 1.00" (15.2 mm x 25.4 mm), #8 (M4) Counterbore</a>   | S1k         |
|                     | <a href="#">SM30TC - Clamp for SM30 Lens Tubes</a>  |             |
|                     | <a href="#">x20 Olympus Objective - UPLSAPO10X2</a>   |             |
|                     | <a href="#">RMSA7 - Adapter with External M26 x 0.706 Threads and Internal RMS Threads</a>            |             |
|                     | <a href="#">CMV10 - C-Mount Adjustable Extension Tube</a>   |             |
|                     | <a href="#">MT-4 Accessory Tube Lens</a>  |             |
|                     | <a href="#">Mitutoyo to C-mount Camera 152.5mm Extension Tube</a>                                     |             |

|  |   |  |
|--|---|--|
|  | <a href="#"><u>NF405-13 - Ø25 mm Notch Filter, CWL = 405 nm, FWHM = 13 nm</u></a> |  |
|  | <a href="#"><u>C-Mount Filter/Polarizer Holder, M6</u></a>                        |  |
|  | <a href="#"><u>25/25.4mm Optic Cell</u></a>                                       |  |
|  | <a href="#"><u>BFS-U3-200S6M-C: 20 MP, 18 FPS, SONY IMX183, MONO</u></a>          |  |
|  | <a href="#"><u>ACC-01-2304: USB3, 1 M, TYPE-A TO MICRO-B LOCKING CABLE</u></a>    |  |
| Breadboard   | <a href="#"><u>Newport Optical Breadboard Table BT-2024<br/>24"x20"x3"</u></a>    |  |
| Custom-printed Components<br><br>(Available via a request to lead authors) | Printing Sample Stage   |  |
|  | M406 Base Plate   |  |
|  | M406 Mount  |  |
|  | Rail Spacer   |  |
|  | Stage Clip  |  |
|  | Stage Mount   |  |
|  | V528 Base Plate   |  |
|  | V528 Mid Plate  |  |
|  | V528 Rail Mount   |  |

180 **Changing focal distance for minimal linewidth.** The below image shows fluorescent microscopy of MCFL filaments of varying linewidth (printed with a  $20 \text{ v v}^{-1}$  % PEGDA, 0.05 mg mL $^{-1}$  LAP, TRITC 0.56 mM solution, scan vel. 100 mm min $^{-1}$ , duty-cycle/PWM 100). Filaments of varying linewidth were achieved through changes to the focus. A minimal linewidth of approximately 7  $\mu\text{m}$  was achieved.

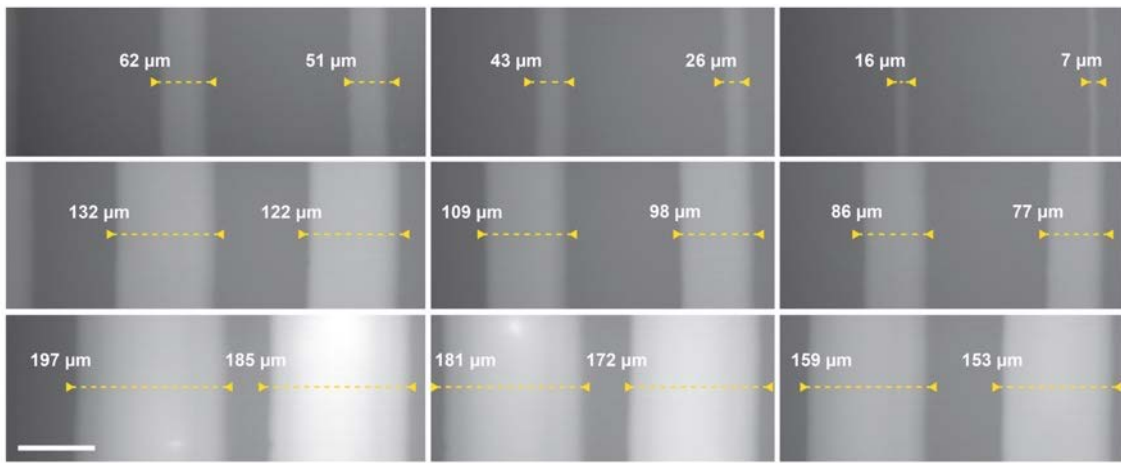


**Figure S4. Changing focus for altering linewidth using MCFL 3DP.**

185 **Attachment assay with bulk hydrogels for various thiol-ene conjugated ligands and cell types.** The broader potential of the thiol-ene chemistry approach was initially tested using different ligands and cell types, including human bone marrow-derived mesenchymal stromal cells (hBDMSCs) and HUVECs (human vascular endothelial cells). The potential of this method was confirmed with bulk hydrogel disks cured with a UV flood lamp using the  
190 photoresist composition used throughout.

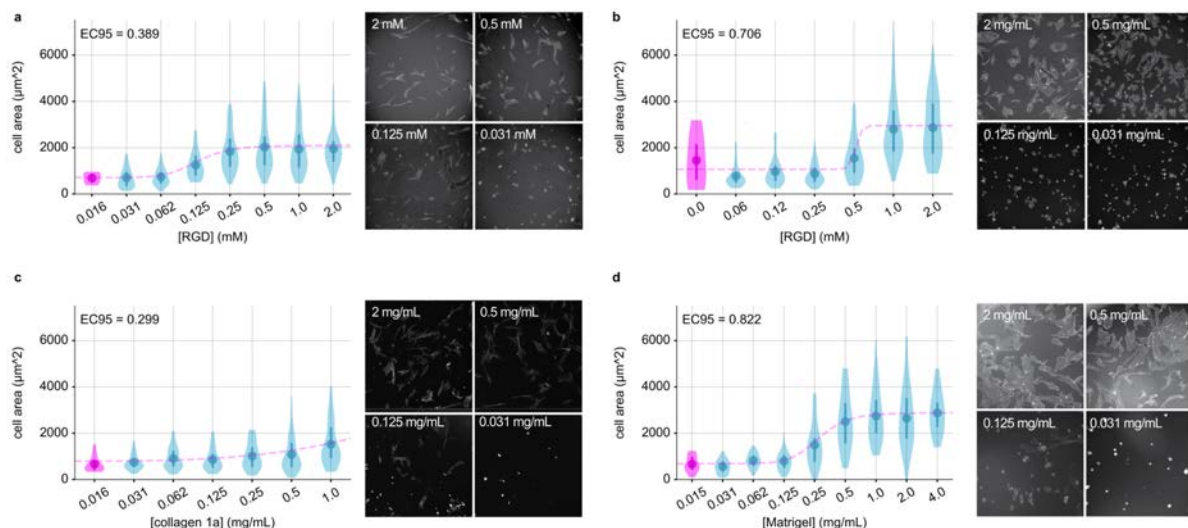


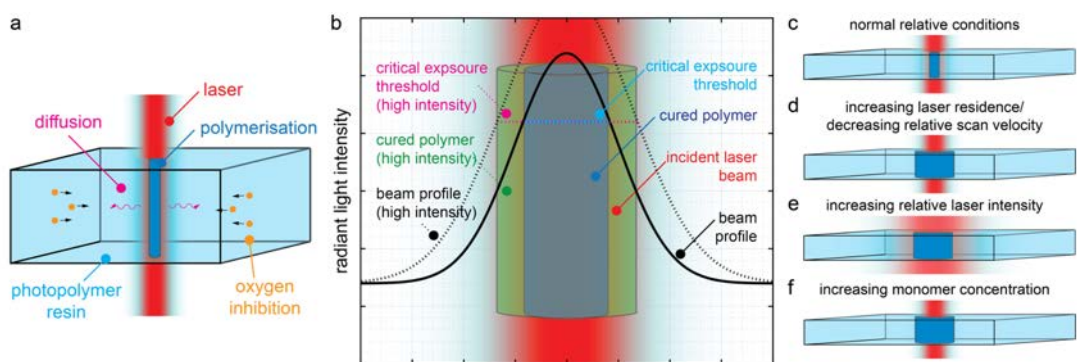
**Figure S5. The thiol-ene bioconjugation approach was first broadly demonstrated for attachment ligands in bulk hydrogels.** Culturing both hBDMSCs and HUVECs for **a**, hBDMSCs with RGD attachment ligand **b**, HUVECs with RGD attachment ligand. **c**, hBDMSCs with rat tail collagen 1A attachment ligand. **d**, HUVECs with Matrigel attachment ligand.  
195 Representative images are shown for phalloidin staining. n >= 12 cells for each experiment.

**Notes on photopolymerization.** We demonstrated that increases to laser scan velocity decreased both Young's modulus and the linewidth of prints (**Figure 2a**), as consistent with a

lowered rate of polymerization due to the decreased light absorption and consequentially lower photoinitiator free radical dissociation (see notes below, **Figure S6**, **Figure S7**)<sup>[21]</sup>.

200 Decreased laser scan velocity and hence increased light absorption are consistent with the effects of increasing the laser power during photopolymerization, where high power yielded increased Young's modulus and linewidth (**Figure 2b**). As a function of the focus, changes to the linewidth were approximated with a linear function that correlated with the diameter of the conic angle of laser transmittance (**Figure 2c**). The relationship between focus and  
205 Young's modulus is nonlinear, a behavior that may be related to photodamage of the niche or interference effects from imperfect optics. Increases in the photoinitiator and monomer concentration produced materials with higher Young's modulus and larger linewidths. This is consistent with accepted photopolymerization models that predict more polymer crosslinking as well as a larger volume exceeding the critical threshold to polymerization for photoresists  
210 with higher monomer and photoinitiator concentration (see notes below, **Figure S6**)<sup>[21]</sup>.

Under irradiation, type I photoinitiators such as the LAP (Lithium phenyl-2,4,6-trimethylbenzoylphosphinate) photoinitiators dissociate into two or more radical species. For type I free radical photopolymerizing systems, a critical exposure threshold exists where a liquid photopolymer is solidified. This occurs when a photoresist absorbs sufficient light  
215 energy, such that free radicals generated from light-induced dissociation of a photoinitiator can overcome free radical inhibition (photoinitiator quenching) to crosslink a monomer and convert it to a solid. Increases to either the incident laser power (See **Figure S6b-f**) or laser residence time (**Figure S6d**) will result in a larger volume of polymerization. i.e., Other factors that alter the critical exposure threshold include changes to the concentration of  
220 photoinitiator, monomer, changes to the reaction atmosphere (changes to ambient [O<sub>2</sub>] and absorbed oxygen radials), radical quenching agents such as glucose oxidase, photobleachers, photoabsorbers, and dyes. As can be observed in **Figure S6b**, changes to the critical exposure threshold result from altering system linewidth.



225 **Figure S6.** Shows a model photoresist during irradiance. **a**, Key interactions are outlined, including laser irradiance and diffusive/oxygen inhibitory species. **b**, The critical exposure threshold and the effect on polymerization and linewidth are shown for varying laser irradiance. A high irradiance results in the polymerization of a larger volume of photoresist. **c**, The effect of varying irradiance is compared, showing changes to the polymerization volume.

230 We examined the effect of changing monomer concentration, photoinitiator concentration, scan velocity, incident light power, and light focus. The standard model of free radical photopolymerization expresses the rate of photopolymerization as<sup>[21]</sup>:

$$R_p = k_p[M] \left( \frac{\Phi \alpha [PI] I_0 10^3 e^{-\alpha[PI]D}}{k_t} \right)^{1/2} \quad (1)$$

235 This expression considers the rate of photopolymerization ( $R_p$ ) as a function of monomer concentration ([M]), photoinitiator concentration ([PI]), and the absorbed light intensity ( $I_0$ ) (where light power, light focus, and scan velocity all alter the absorbed light intensity). The remaining variables in Equation 1 above are ( $D$ ) the depth of penetration, ( $\alpha$ ) the absorption coefficient or molar absorptivity, ( $\Phi$ ) the quantum yield for initiation or number of propagating chains initiated per light photon absorbed, ( $k_p$ ) rate constant for polymer chain propagation and ( $k_t$ ) termination rate constant. This model reveals a high sensitivity to 240 changes in the photoinitiator concentration, as per the exponential term  $e^{-\alpha[PI]D}$ .

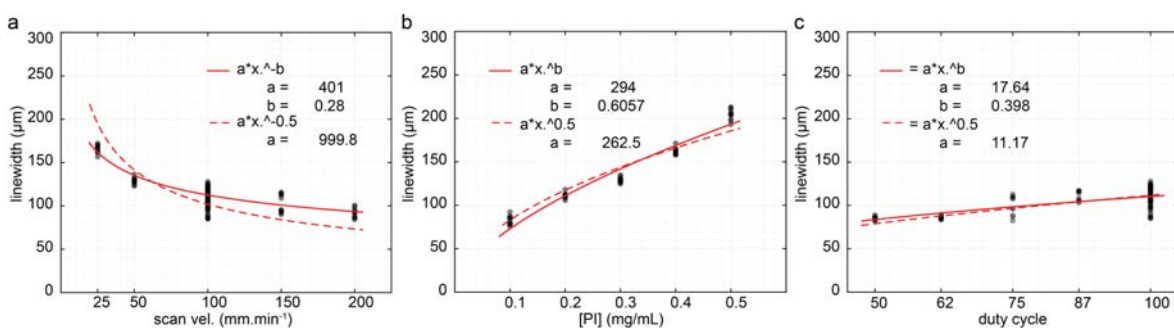
Accordingly, uniformity in a photoresist is best achieved using as low of a concentration of a photoinitiator as possible, such that the exponent approximates 0. Thus, thin reaction systems ( $D \sim 0$ ) with low photoinitiator concentrations ( $[PI] \sim 0$ ) are reduced such that the exponent  $\alpha[PI]D \sim 0$ , and the expression reduces such that:

245  $R_p \propto [M]; R_p \propto I_0^{1/2}; \text{ and } R_p \propto [PI]^{1/2} \quad (2)$

As the photopolymerization rate relates to the critical exposure threshold, so does it relate to the linewidth since polymerization occurs in this region. Changes to the scan velocity are inversely proportional to the absorbed light intensity (moving twice as fast would half the light exposure); this predicts that the linewidth and scan velocity should exhibit a ½-order 250 relationship. However, fitting the data presented in **Figure 2** with this model does not approximate the observed behavior (see **Figure S6a** below). Alternatively, fitting the data to an unknown order reveals the 0.28<sup>th</sup> order. This shows complex interactions that the model does not account for, suggesting that the criterion of low [PI] and D is not met for the MCFL device herein. Similar to changes in scan velocity, we fit the observed linewidth as a function 255 of the photoinitiator and light power/duty-cycle. Fitting the data presented in **Figure 2** with

the above model better approximates the observed behavior (see **Figure S6b-c** below). Otherwise, fitting data to an unknown order reveals the photoinitiator concentration approximates a 0.61<sup>th</sup> order relationship with linewidth, and the laser duty-cycle approximates a 0.40<sup>th</sup> order relationship with linewidth. Considering the effects of diffusing radical species as well as changes to the concentration of inhibiting species such as that from ambient oxygen could help explain these observations. This analysis demonstrates that photoresist systems are highly sensitive, nonlinear, and difficult to predict. Accordingly, it is reasonable that photoresist property prediction is limited to using unique empirical models developed for each photoresist and device.

265



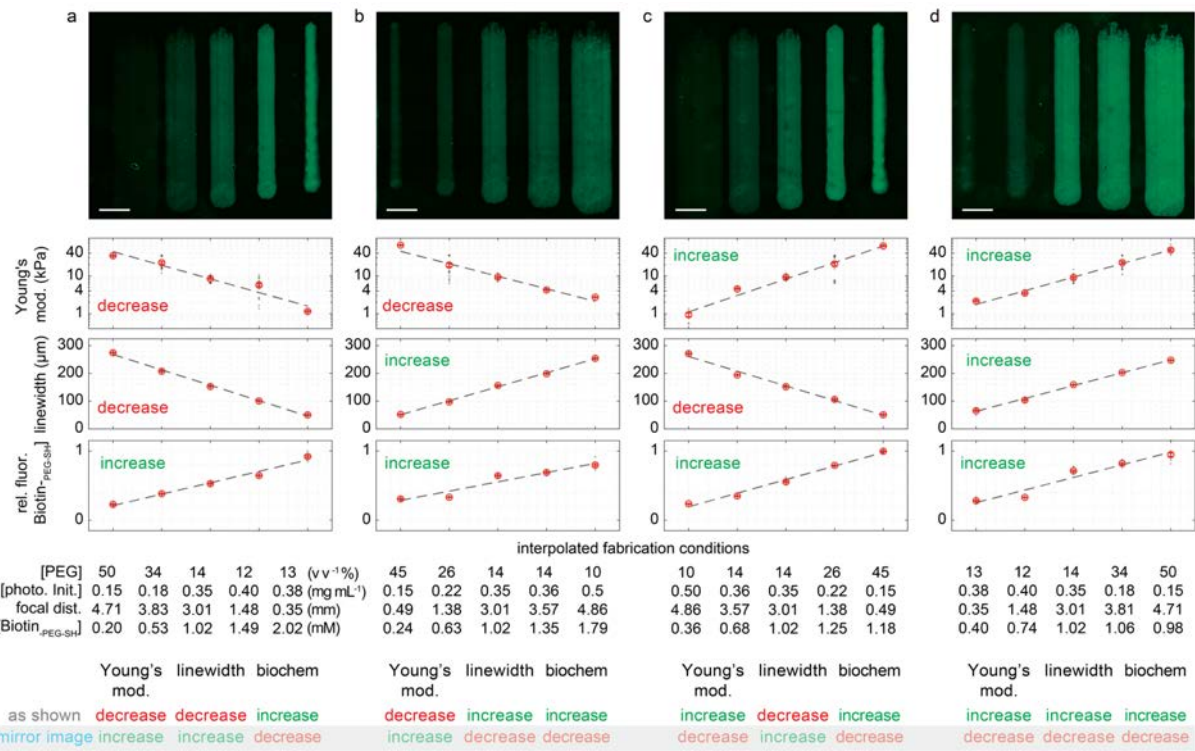
270

**Figure S7.** The analysis of the FL variables of scan velocity, photoinitiator concentration, and duty-cycle on the resulting polymerized linewidth. The relationship between variables is explored in the context of the standard model of photopolymerization simplified in equation 5, for which the variables should approximate a  $\frac{1}{2}$  power relationship with linewidth. The deviations from  $\frac{1}{2}$  order show that simplifications can not be applied (sufficiently low [PI] and  $D$  is not met) with additional potential complexities, including that from inhibitory and diffusive species. This exemplifies the complexity of dependent variable prediction for photopolymerization.

275

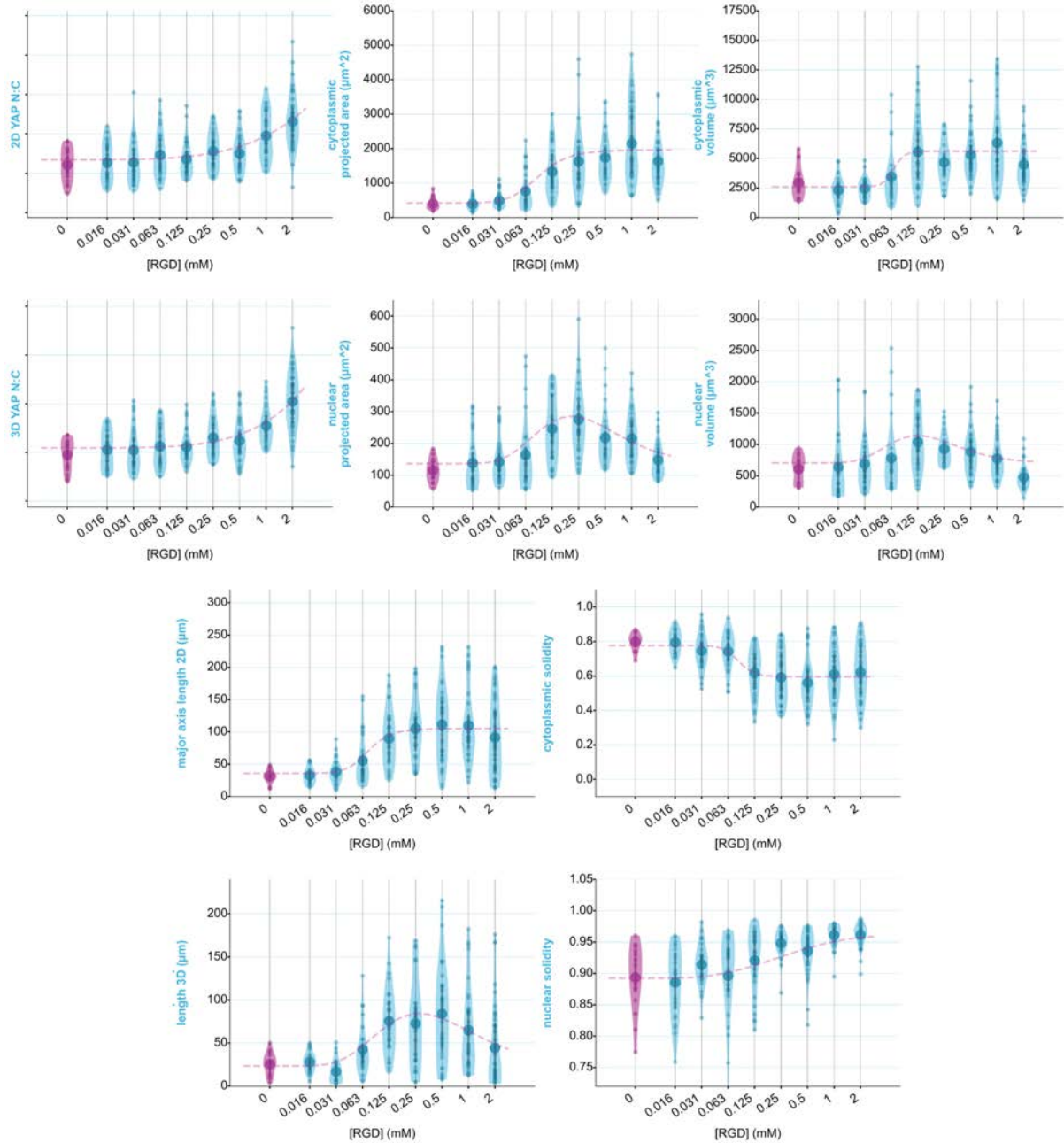
280

**Generating niches from interpolated properties.** To demonstrate the utility of this method, we printed niche filament arrays with adjacent filaments of increasing or decreasing relative Young's modulus, linewidth, and relative bioconjugate fluorescence (**Figure S8**). While eight possible permutations with parallel and anti-parallel changes to the three dependent variables are possible (**Figure S8**), four were fabricated, as the remaining permutations constitute the mirror-images of those shown (i.e., can be printed by simply reflecting print order, rather than the conditions of fabrication). The fabrication conditions are tabulated at the figure base with properties interpolated on the dotted lines-of-best-fit. Accordingly, the deviation from lines-of-best-fit as seen in the experiment (as run in triplicate), reflect the reproducibility of the method and precision for achieving arbitrarily interpolated material properties. These deviations likely represent the complex non-linear behaviors observed in photochemical reactions as discussed above.



285 **Figure S8.** Shows microstructured niches generated with interpolated properties from the reduced state-space, with  
interpolation of the different permutations of the 3 dependent variables either increasing and decreasing in a parallel and  
antiparallel fashion. At the figure base is the key relating permutation 'mirror images' explicitly, i.e., superposition by  
reflecting print order.

290 **Observations of hADSC morphology on [RGD] microstructured niche filaments.** In  
addition to the characterization of YAP N:C (**Figure 3**, **Figure S9**), the confocal microscopy  
of human adipose-derived stromal cells (hADSCs) completed over filaments of differing  
[RGD] allowed the characterization of cell morphological parameters. The below graphs  
supplement the data provided in **Figure 3**, showing that structured [RGD] altered a range of  
morphological parameters, including: the projected cytoplasmic area (**Figure S9b**), including  
295 cytoplasmic volume (**Figure S9c**), nuclear-projected area (**Figure S9e**), nuclear volume  
(**Figure S9f**), major axis length 2D (**Figure S9g**), cytoplasmic solidity (**Figure S9h**), longest  
axis length 3D (**Figure S9i**), nuclear solidity (**Figure S9j**). In general, these quantitative  
morphological characterizations show that increases to [RGD] led to cells with more  
elongated shapes of larger areas and volume.



300

**Figure S9.** Morphological properties of ADSCs as adherent to different [RGD]-structured niche filaments.

**Niche fabrication conditions with defined linewidth, RGD, Young's modulus, and BMP2, as well as bone-fat and germ-layer tissue assemblies.** The below tabulates the interpolated fabrication conditions used to generate the various niche arrays throughout this work.

305

**Table S 2.** Specific photoresist and MCFL 3DP variables used for fabrication of FL hydrogels with variable Young's modulus, RGD and BMP2 concentrations. All niches were printed interpolating the state-space shown in **Figure 2g-i**, with fixed laser power of 100% PWM of the 150 mW Cobolt 06-01, and a scanning velocity of 100  $\mu\text{m min}^{-1}$ .

| Label                       | [RGD] (mM)                               | Young's mod.<br>(kPa) | [BMP2]<br>(ng/mL) | linewidth<br>( $\mu\text{m}$ ) | PEG<br>(v $\text{v}^{-1}$<br>%) | [LAP]<br>( $\text{mgmL}^{-1}$ ) | focus<br>(mm) | biochemical<br>modifier |
|-----------------------------|--|-----------------------|-------------------|--------------------------------|---------------------------------|---------------------------------|---------------|-------------------------|
| <b>Fig 1hj</b>              |  |                       |                   |                                |                                 |                                 |               |                         |
| 3D structures               | (photoabsorber/<br>Tartrazine = 3<br>mM) | -                     | -                 | 250                            | 24.16                           | 0.23                            |               |                         |
| <b>Fig 3a</b>               |  |                       |                   |                                |                                 |                                 |               |                         |
| 50 $\mu\text{m}$            | 4.4732/0                                 | 8                     | 0                 | 50                             | 24.99                           | 0.22                            | 0.5326        | 1.1183                  |
| 100 $\mu\text{m}$           | 4.8556/0                                 | 8                     | 0                 | 100                            | 13.18                           | 0.36                            | 1.5128        | 1.2139                  |
| 150 $\mu\text{m}$           | 4.5364/0                                 | 8                     | 0                 | 150                            | 13.60                           | 0.35                            | 3.0025        | 1.1341                  |
| 200 $\mu\text{m}$           | 4.1108/0                                 | 8                     | 0                 | 200                            | 21.85                           | 0.25                            | 4.3207        | 1.0277                  |
| 250 $\mu\text{m}$           | 4/0                                      | 8                     | 0                 | 250                            | 24.16                           | 0.23                            | 5.0718        | 1                       |
| <b>Fig 3c, Fig<br/>4c,d</b> |  |                       |                   |                                |                                 |                                 |               |                         |
| stiff-1                     | 1.2651                                   | 20                    | 0                 | 250                            | 35.22                           | 0.17                            | 4.9879        | 0.84341                 |
| stiff-2                     | 1.3415                                   | 15                    | 0                 | 250                            | 31.57                           | 0.18                            | 5.0295        | 0.89435                 |
| stiff-3                     | 1.4816                                   | 10                    | 0                 | 250                            | 25.07                           | 0.22                            | 5.0552        | 0.98771                 |
| stiff-4                     | 1.6872                                   | 5                     | 0                 | 250                            | 15.25                           | 0.32                            | 4.9684        | 1.1248                  |
| stiff-5                     | 1.7346                                   | 2.5                   | 0                 | 250                            | 12.92                           | 0.36                            | 4.9320        | 1.1564                  |
| <b>Fig 3b, Fig<br/>4a,b</b> |  |                       |                   |                                |                                 |                                 |               |                         |
| rgd-1                       | 8  | 8                     | 0                 | 250                            | 24.16                           | 0.23                            | 5.0718        | 1                       |
| rgd-2                       | 2  | 8                     | 0                 | 250                            | 24.16                           | 0.23                            | 5.0718        | 1                       |
| rgd-3                       | 0.5                                      | 8                     | 0                 | 250                            | 24.16                           | 0.23                            | 5.0718        | 1                       |
| rgd-4                       | 0.125                                    | 8                     | 0                 | 250                            | 24.16                           | 0.23                            | 5.0718        | 1                       |
| rgd-5                       | 0.03125                                  | 8                     | 0                 | 250                            | 24.16                           | 0.23                            | 5.0718        | 1                       |
| rgd-6                       | 0  | 8                     | 0                 | 250                            | 24.16                           | 0.23                            | 5.0718        | 1                       |
| bmp2-1                      | 2  | 8                     | 0                 | 250                            | 24.16                           | 0.23                            | 5.0718        | 1                       |
| bmp2-2                      | 2  | 8                     | 1.6               | 250                            | 24.16                           | 0.23                            | 5.0718        | 1                       |
| bmp2-3                      | 2  | 8                     | 8                 | 250                            | 24.16                           | 0.23                            | 5.0718        | 1                       |
| bmp2-4                      | 2  | 8                     | 40                | 250                            | 24.16                           | 0.23                            | 5.0718        | 1                       |
| bmp2-5                      | 2  | 8                     | 200               | 250                            | 24.16                           | 0.23                            | 5.0718        | 1                       |
| bmp2-6                      | 2  | 8                     | 1,000             | 250                            | 24.16                           | 0.23                            | 5.0718        | 1                       |
| <b>Fig 4i,j,k</b>           |  |                       |                   |                                |                                 |                                 |               |                         |
| bone $\mu$ struc            | 3.5774                                   | 15                    | 894.3             | 250                            | 31.57                           | 0.18                            | 5.0295        | 0.8944                  |
| fat $\mu$ struc             | 4.6256                                   | 2.5                   | 0                 | 250                            | 12.92                           | 0.36                            | 4.9320        | 1.1564                  |
| <b>Fig 5</b>                | <b>Matrikel<br/>(v/v%)</b>               |                       |                   |                                |                                 |                                 |               |                         |
| dev. org.-1                 | 50                                       | 1                     | -                 | 250                            | 10                              | 0.25                            | 4.98864       | -                       |
| dev. org.-2                 | 50                                       | 6                     | -                 | 250                            | 12.6                            | 0.25                            | 5.02664       | -                       |
| dev. org.-3                 | 50                                       | 11                    | -                 | 250                            | 15.3                            | 0.25                            | 5.06464       | -                       |
| dev. org.-4                 | 50                                       | 30                    | -                 | 250                            | 18                              | 0.25                            | 5.10264       | -                       |
| dev. org. uniform           | 50                                       | 11                    | -                 | 250                            | 15.3                            | 0.25                            | 5.02664       | -                       |
| <b>Fig 6</b>                |  |                       |                   |                                |                                 |                                 |               | <b>[BMP4]</b>           |
| dev.org.bmp4-400            | 50                                       | 11                    | -                 | 250                            | 15.3                            | 0.25                            | 5.02664       | 400 ng/mL               |
| dev.org.bmp4-0              | 50                                       | 11                    | -                 | 250                            | 15.3                            | 0.25                            | 5.02664       | 0 ng/mL                 |

310

**Representative images of MCFL bone-fat niches, with channels separated to observe mineralization.** Bone-fat niches were imaged following the multiplexing detection of bone

and fat markers. This combined LipidTOX together with the CNA35 Collagen 1A stain, a well-established marker of mature bone<sup>[22]</sup>. Methods characterizing mineralization were not possible due to an inability to multiplex bone mineralization with Alizarin Red (AZR) staining, together with LipidTOX, due to the shared red fluorescence of LipidTOX and AZR. Below we show 3 representative images of the bone-fat microtissues, with channels LipidTOX (red), DNA/Hoechst (blue), CNA35 (green), and the brightfield images separated (Figure S10). Arrows show prominent dark ring regions of the brightfield images where mineralization was observed.

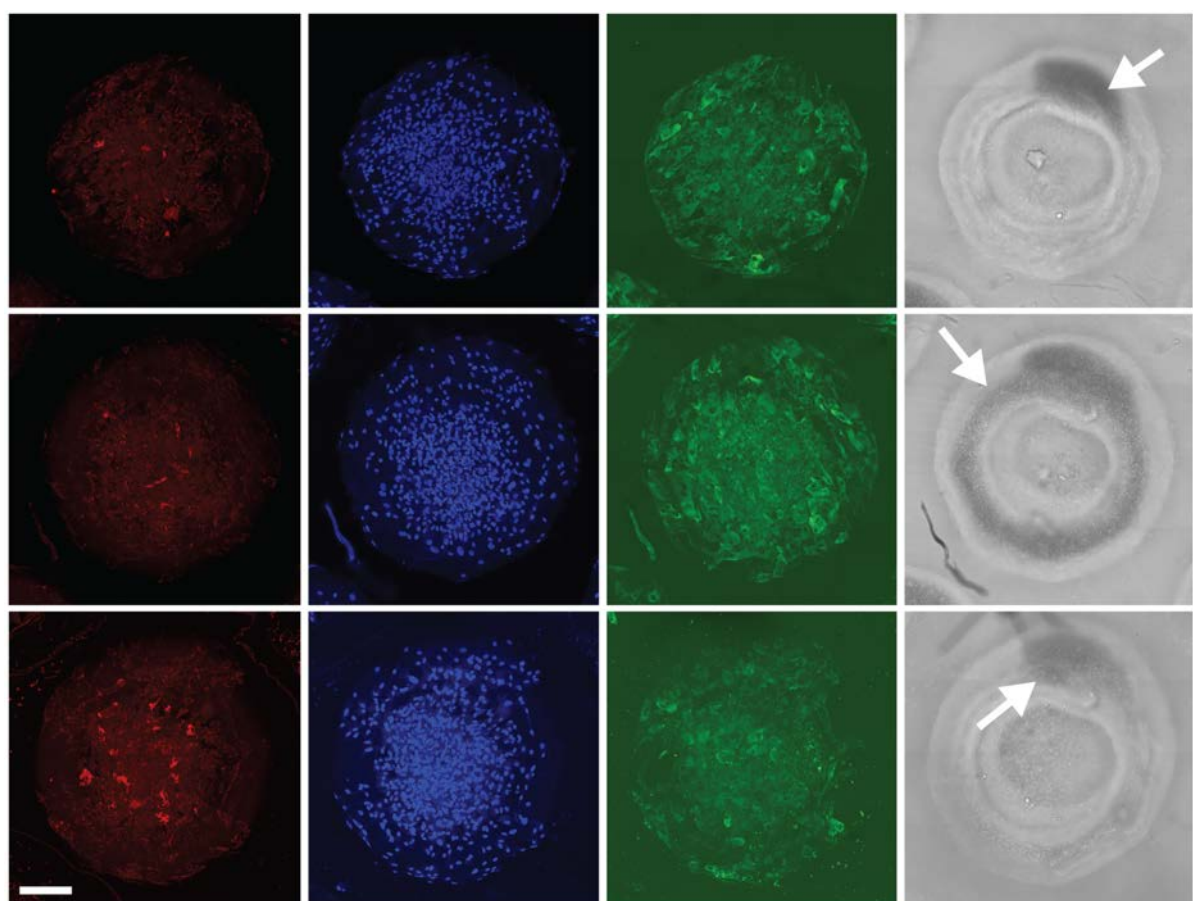
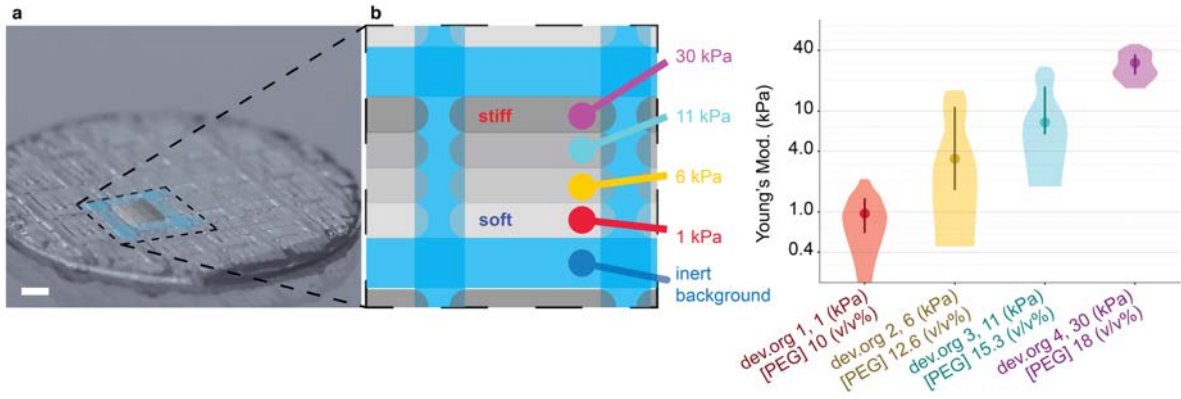


**Figure S10.** Representative images of bone-fat niches with 4 channels separated. Dark regions and arrows indicate region of high mineralization. Gamma corrected for improved visibility of low brightness regions. Scale bar 200  $\mu$ m.



325 **Figure S11.** Force spectroscopic characterization of specific microproperties of mechano-structured niche squares. Mechano-structured array as fabricated for characterization with AFM. **a**, Macro-lens photography of niche array alongside **b**, schematic of structured mechanical microproperties. **c**, niche properties as measured by AFM force spectroscopy. Scale bar 1 mm.

330 **Generation of immunofluorescent marker expression maps.** The expression maps in **Figure 5-6** pool data of marker expression across replicates into a single plot. This was achieved as outlined graphically in the below **Figure S12**. First, confocal scans were taken for each marker of interest, as well as the Hoechst nuclear stain, used to generate a mask for each nucleus (**Figure S12, step 1**). Using a 3D adaption of the StarDist segmentation tool<sup>[23,24]</sup>, masks for single nuclei were identified (**Figure S12, steps 2-3**). Using the nuclei 335 masks, the mean fluorescent intensity for each channel and nuclei was then calculated (**Figure S12, step 4**). For the YAP N:C ratio measured in hiPSCs, the cytoplasmic mask was defined by dilating the nuclear volume by half the nucleus volume equivalent radius and subtracting all nuclear masks. Then with the respective mean fluorescent intensity of each marker per nuclear or cytoplasmic masks, the coordinates of each nucleus within the niche 340 are calculated. Linear transformations of each mask's coordinates were mapped to universal coordinates to correct rotational and translational imprecisions when imaging replicates (**Figure S12, step 5**). This produced a data set with coordinates and marker intensity for each nucleus (**Figure S12, step 6**). Further, experimental replicates and immunostained markers that could not be multiplexed could be pooled, plotted, and compared (**Figure S12, step 7**). 345 3D scatter and surface plots as shown in **Figures 5-6** and **Figure S12-15, S21, S23** were then generated using matplotlib. Within plots, each dot represents a single cell with the height, size, and transparency of the dot scaled to the normalized fluorescent intensity of the marker across replicates, with further normalization on the total dot area in each plot. Surface plots were then fit to the local mean of the marker expression for the given scatter plot. 350 Additionally, to limit crowding, the number of dots/cells was limited to 200,000, with cells

chosen randomly to this limit if exceeded. Further, for merge plots where multiple markers are shown simultaneously, a maximum number of 60,000 cells selected at random are shown for each marker. 3D scatter, and surface plots are shown alongside representative fluorescent microscopy, for which saturation correction has been applied for improved visibility.

355 Specifically, clipping and linear normalization to a maximum saturation of a 98% percentile bit-depth value used for the representative confocal MIP images shown in **Figure 5**, **Figure 6**, and all supplemental figures showing hiPSCs.

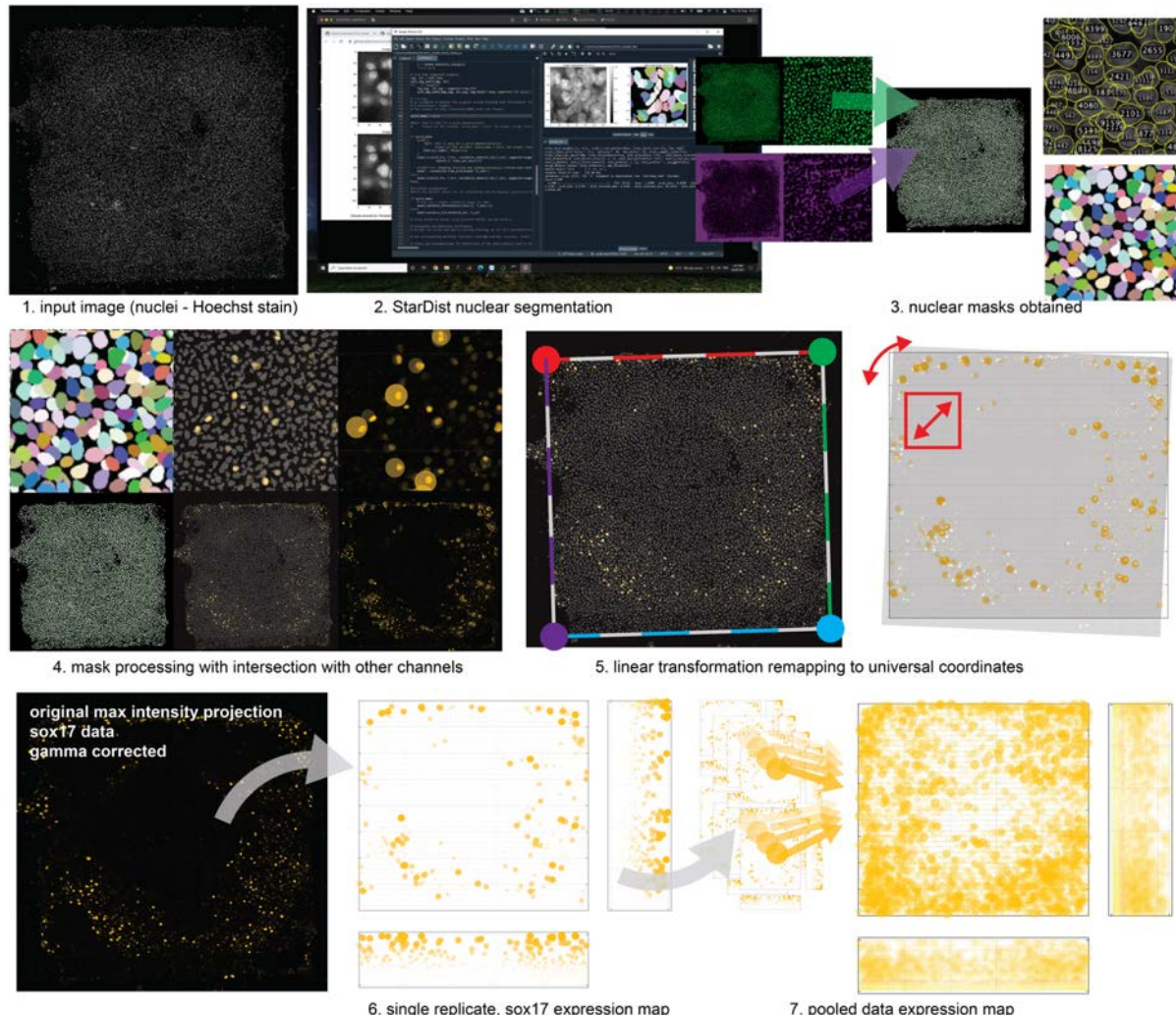


**Figure S12.** Overview of characterization method used to generate tissue expression maps with pooled and mapped data across replicates.

360 **Replication and comparison of tissue patterning with circular glass-control experiments.** To establish a protocol for using niches with structured microproperties, we first aimed to replicate the seminal work in embryonic micropatterning completed by

365 Warmflash et al. 2015<sup>[25]</sup>. We first replicated the patterning of germ-layer derivatives in  
circular tissue micropatterns *in vitro*, with the culture of hiPSCs (HPSI0314i-hoik\_1) plated  
on a Matrigel-coated glass 1000  $\mu\text{m}$  diameter circular adhesive templates, with boundaries  
defined using inert photo-printed PEG (**Figure 5a**). Cells were seeded in Essential 8 Flex  
media, with CEPT cocktail<sup>[26]</sup> for 2 h as per method indicated on **Figure 5** and **Figure 6**  
370 respectively. Cells cultured on the homogenous circular template generated radially  
symmetric germ-layer derivatives (**Figure S13**). Measuring tissue-patterning with progenitor  
cells of the mesoderm (BRA-positive), endoderm (SOX17-positive), and ectoderm (SOX2-  
positive) at 48 h revealed a phenotype equivalent to the Warmflash work's time point at 24-30  
h. Accordingly, the endpoint of our protocol was extended from 48 h to 72 h. **Figure S13**  
375 below compares 48 h and 72 h time points, showing representative images, alongside the  
pooled-position-mapped marker expression. At 48h, expression of SOX17 was only found at  
the periphery, with maximum intensity levels comparable to background staining. Further,  
BRA expression was only apparent in the most peripheral cells. The extension of our  
endpoint to 72 h produced BRA expression became relatively centralized, and SOX17  
380 expression became prominent from the background levels. In subsequent experiments  
exploring the use of niche mechano-chemical properties for directing cell fate decisions, the  
endpoint was extended to 72 h, except for **Figure S15** below, showing tissue patterning  
marker expression in mechano-structured niches at 48 h.

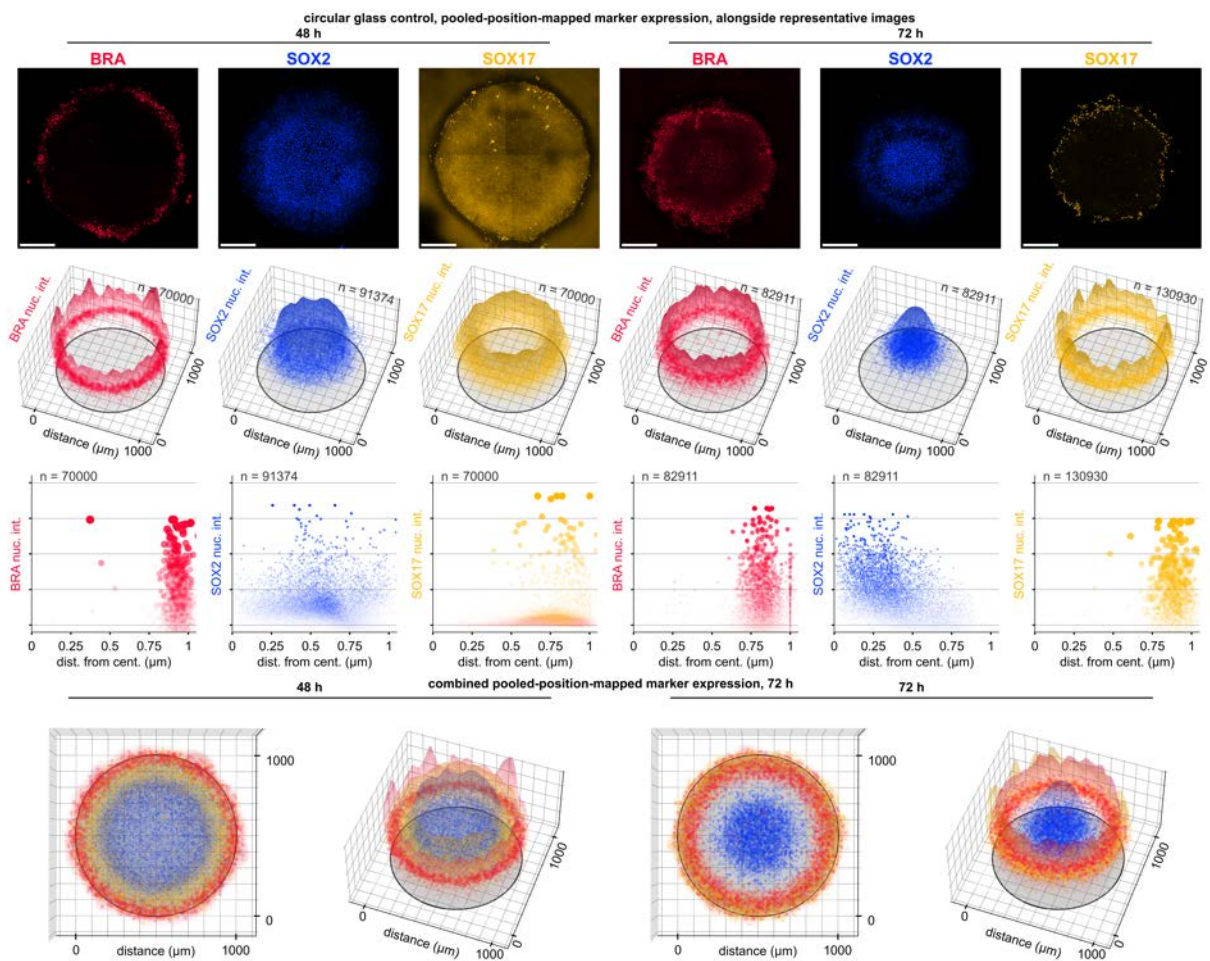


**Figure S13. Comparison of hiPSC culture endpoint by replicating circular glass-control experiments.** Row 1 shows representative images of circular templated germ-layer tissue patterning with Matrigel-coated-glass and inert printed template boundaries. Immunofluorescent staining of templates 48 h (three panels at the left) and 72 h (three panels at the right) post-BMP4-treatment (50 ng/mL), showing (mesoderm: BRA, red; ectoderm: SOX2, blue and endoderm: SOX17, yellow). For improved visibility, images are shown with linear-scaling and clipping to a maximum saturation of a 98% percentile bit-depth value. Scale bar 200  $\mu$ m. **Row 2** shows position-mapped expression graphs of replicate pooled-data for respective markers labeled directly above, with dot color and size scaled as described in the supplementary information above. **Row 3** shows the marker expression intensity projected along the radial dimension of the circular pattern. Each dot represents a single cell with color and size scaled as described in the supplementary information above. **Row 4** shows two views of tissue patterning at both 48 h (two panels at the left) and 72 h (two panels at the right), as shown in *Row 2*, with corresponding markers overlaid on a single plot. Notably, the 72 h endpoint shows similar tissue patterning to Warmflash et al. obtained at 48h.

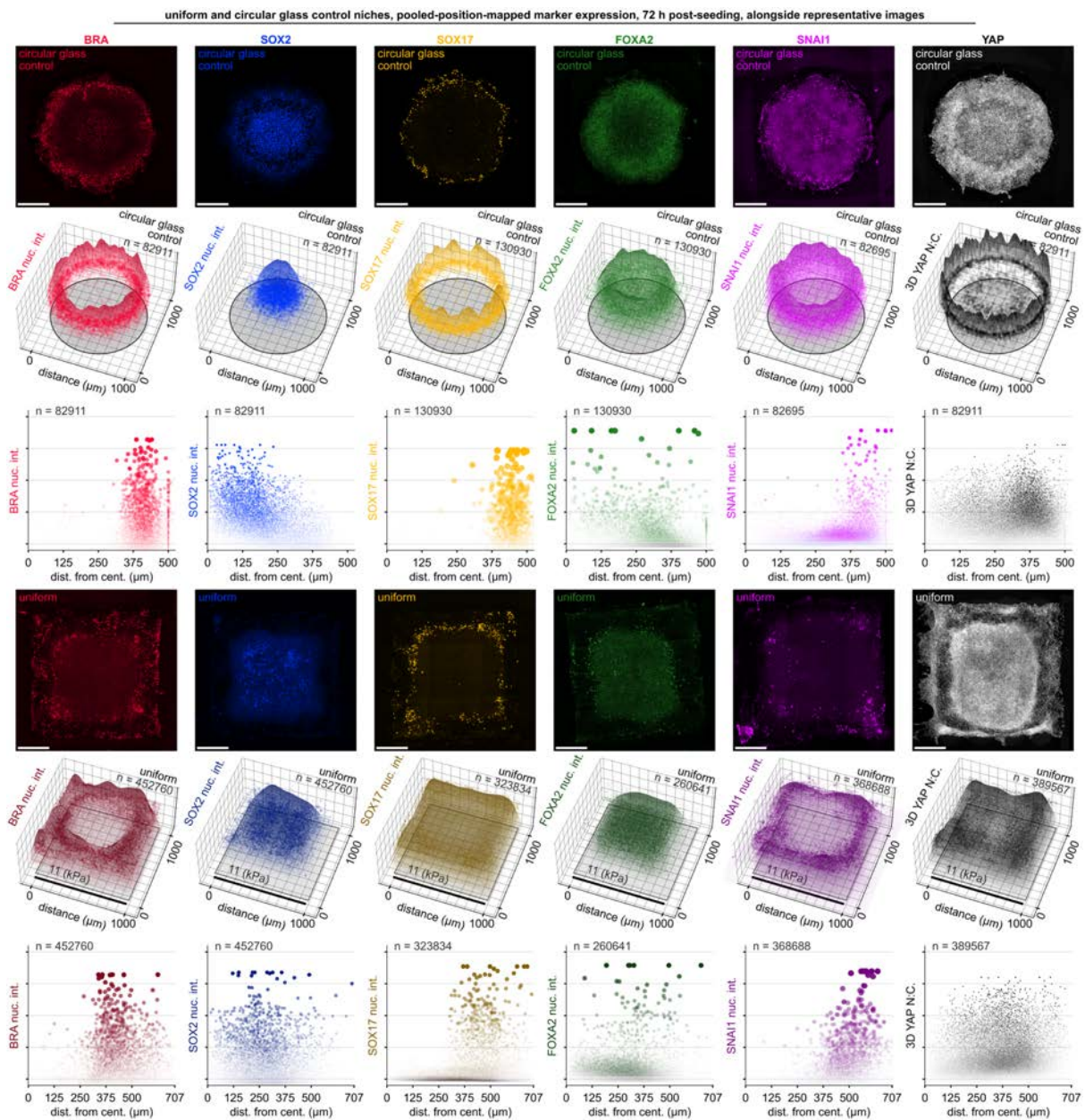
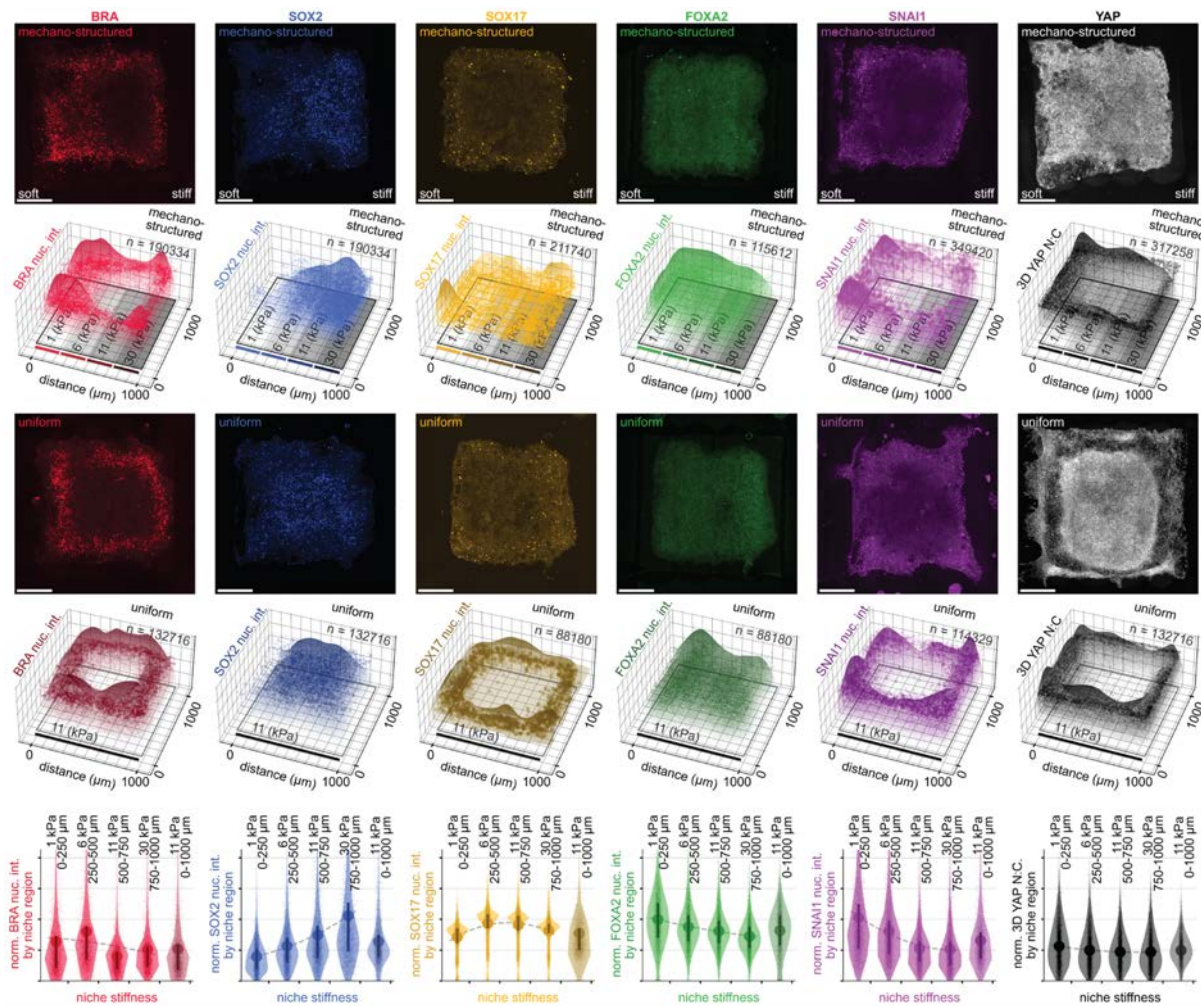


**Figure S14. Comparison of circular glass control niches with square uniform niches at 72 h.** **Rows 1 and 4** show representative images over circular glass and uniform niches at 72 h for the markers: BRA (red), SOX2 (blue), SOX17 (yellow), FOXA2 (green), SNAI1 (purple), YAP (grey). The overlaid text indicates the underlying niche type. **Rows 2 and 5**, Show replicate data presented as 3D scatter and surface plots overlaid on a representation of the corresponding niche. **Rows 3 and 6**, Shows plots with reduced dimensionality, projecting the mapped x/y position into the single dimension - distance from the center of the niche. Distance from the center of the niche is plotted against the relative fluorescence intensity of the given marker. The horizontal axis for circular plots extends to 500  $\mu\text{m}$  in row 3, extending to 707  $\mu\text{m}$  for square plots (the maximum distance possible from the center of a square with 1000  $\mu\text{m}$  edges). Patterning over the circular glass and uniform niches are similar, with peripheral mesodermal and endodermal markers.

In addition to the characterization of a range of marker expression levels over niches with uniform or mechano-structured properties at an endpoint of 72 h, we stained and

characterized niches at 48 h. Mechano-structured niches were fabricated with a 1D gradient in their mechanics as per **Figure 5** of the main article (**Figure 5d**) alongside a control niche 410 with uniform microproperties (**Figure 5a**). hiPSCs cultured on both niche types were induced to differentiate with BMP4 (50 ng/mL) into progenitor cells of the mesoderm (BRA-positive), endoderm (SOX17-positive), and ectoderm (SOX2-positive)<sup>[25]</sup>. Image analysis pooling replicate-data (**Figure S12**) revealed that hiPSCs cultured on uniform stiffness substrate displayed regionalization of germ layer tissues from their center-to-periphery 415 (**Figure 5c,j,i,k**), similar to that observed for circular micropatterns (**Figure S13**)<sup>[25]</sup>. In contrast, cells cultured over mechano-structured niches were able to reconfigure the tissue pattern. Expression of BRA- and SOX17-positive cells were localized to niche regions of low stiffness and SOX2-positive cells to regions with high stiffness (**Figure 5f,h,l**). This observation is consistent with the patterning observed at 72 h.

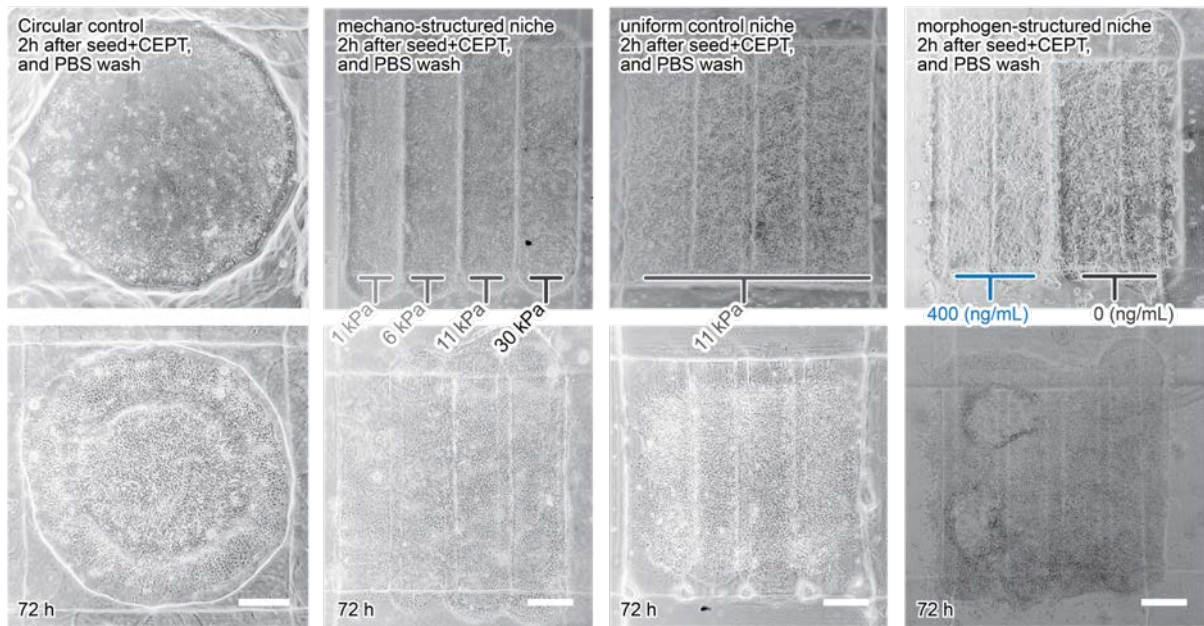


420

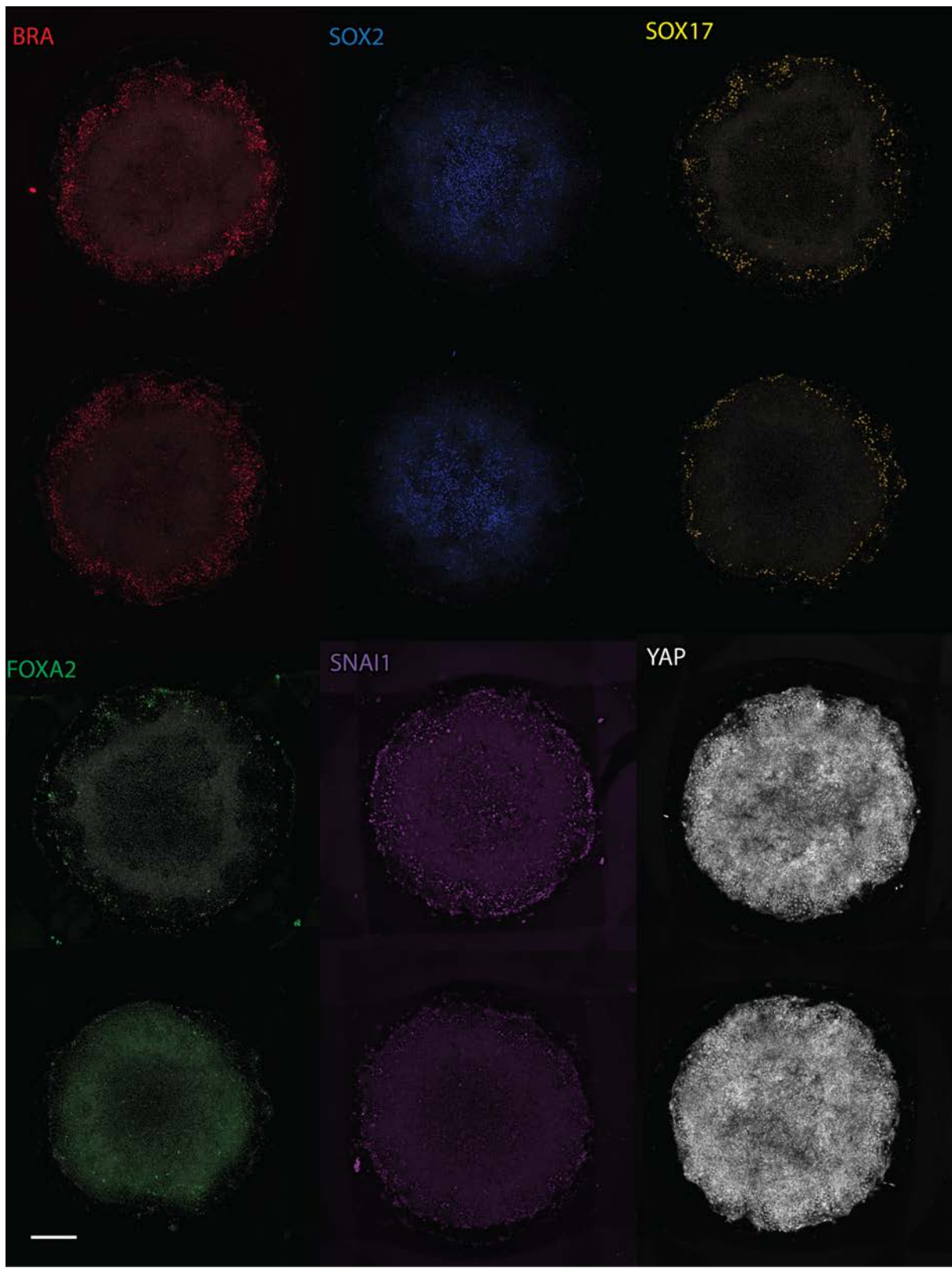
**Figure S15. Niche-mechanics directed marker expression at 48 h.** **Rows 1 and 3** shows representative images over mechano-structured and uniform niches at 48 h for the markers: BRA (red), SOX2 (blue), SOX17 (yellow), FOXA2 (green), SNAI1 (purple), YAP (grey). Overlaid text indicates image orientation of the niche type. The color-coding has saturation

correction applied to representative images, with clipping and linear normalization to a maximum saturation of a 98%  
425 percentile bit-depth value applied for improved visibility. Image overlay labels the mechanical properties over the different niches. The orientation of niches: soft-to-stiff mechanical gradient (left-to-right). Scale bar, 200  $\mu$ m. **Rows 2 and 4**, Replicate data presented as 3D scatter and surface plots overlaid on the corresponding niche. Surface plots are fit to the local mean of the marker expression and plotted on a separate axis to the scatter plots. Each dot represents a single cell with the size and transparency of the dot scaled to the normalized fluorescent intensity of the marker across replicates. **Row 5**, Violin plots  
430 comparing the mean and distribution difference, including mean and 1<sup>st</sup>/3<sup>rd</sup> quartile lines of replicate data as mapped to respective niche regions indicated on the x-axis.

**Figure S16** below shows brightfield imaging of the four different niches used in this work with hiPSCS. Text overlays describe the niche properties, which are consistent between rows.  
435 **Figure S16 Column 1** shows the circular glass control micropatterns. Following the seeding step, leaving cells to attach for 2 h with the pharmacological cocktail CEPT, hiPSCs at the center of the colony exhibit tight junctions characteristic of hiPSCs. At 72 h, a circular ring structure of the cells appears along the radius of the structure - consistent with the appearance of cells in predicate work<sup>[25]</sup>. **Figure S16, Column 2** shows brightfield imaging of cells attached to morphogen-structured niches. Relative to other niches, the lower seeding density  
440 used for morphogen- structured niches (450 k cells per cm<sup>2</sup>) is evident. The 72 h time point shows the formation of circular node-like structures occupied by large cells over BMP4 containing regions, with more densely packed and smaller cells over regions absent of BMP4.  
**Figure S16, Column 3** shows brightfield microscopy of mechano-structured niche structures. The boundary of the niche pattern exhibits larger, less densely packed cells which bias  
445 towards the softer regions of the substrate. Compared to the soft regions on the left, the stiff boundary at the right exhibits relatively small cells with dense packing. When compared with the uniform niche, cell morphology and density are symmetric around the square structure.



450 **Figure S16. Brightfield image of the four different niches at 2 and 72 h. Row 1** Representative images of niches at 2 h, with text overlays describing the niche properties that are consistent between rows. **Row 2** Niches at 72 h. **Column 1** circular glass control experiments. **Column 2** mechano-structured niches. **Column 3** uniform niches. **Column 4** morphogen-(BMP4)-structured niches.



455 **Figure S17. High resolution images of representative circular control niches at 72 h.** High magnification images of marker expression at 72 h, overlaid on gray nuclear stain. Scale bar, 200  $\mu$ m. The color-coding has saturation correction applied to above images, with clipping and linear normalization to a 99.8% percentile bit-depth for improved visibility.

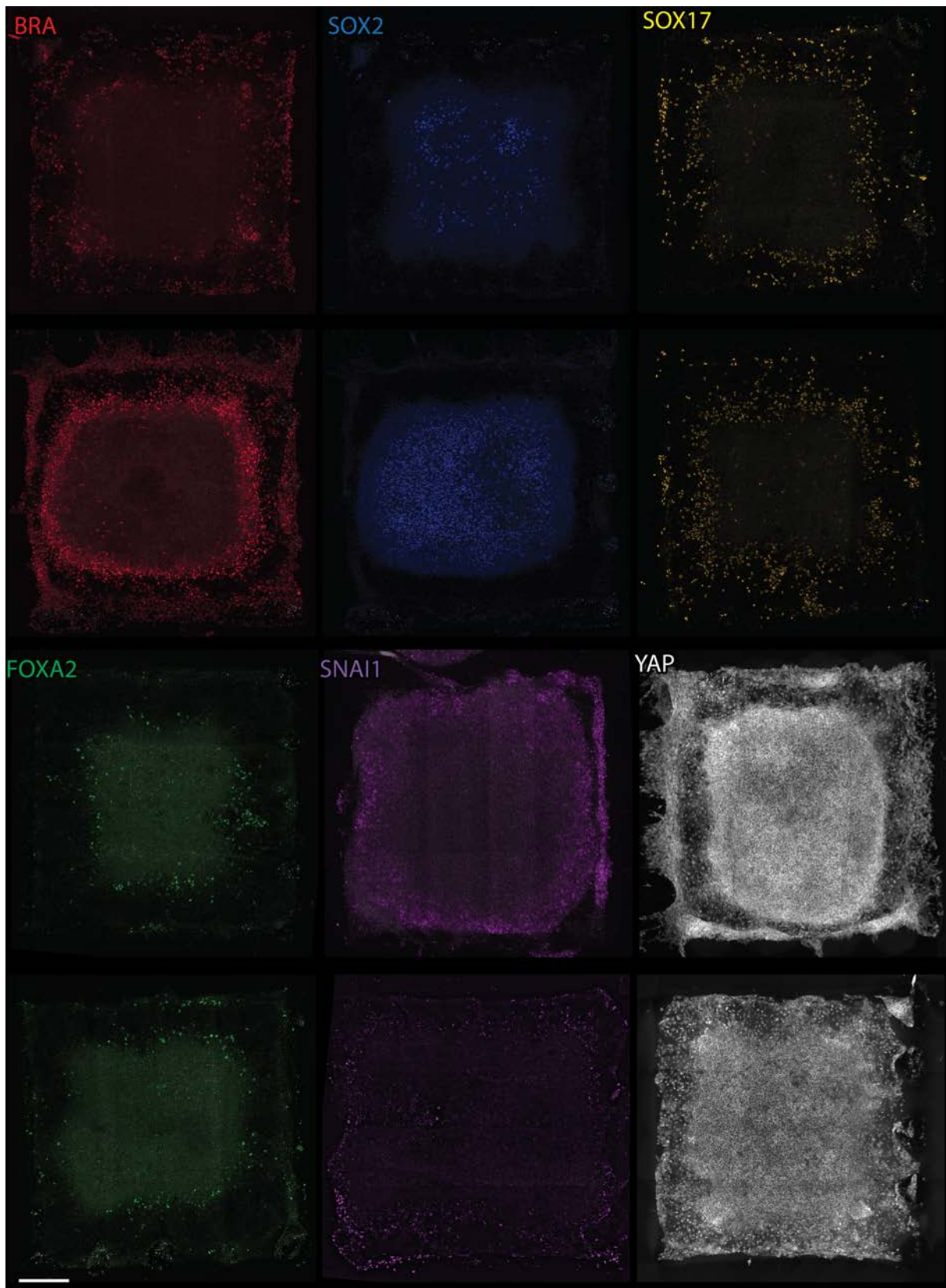


**Figure S18. High resolution images of representative uniform control niches at 72 h.** High magnification images of marker expression at 72 h, overlaid on gray nuclear stain. Scale bar, 200  $\mu$ m. The color-coding has saturation correction applied to above images, with clipping and linear normalization to a 99.8% percentile bit-depth for improved visibility.

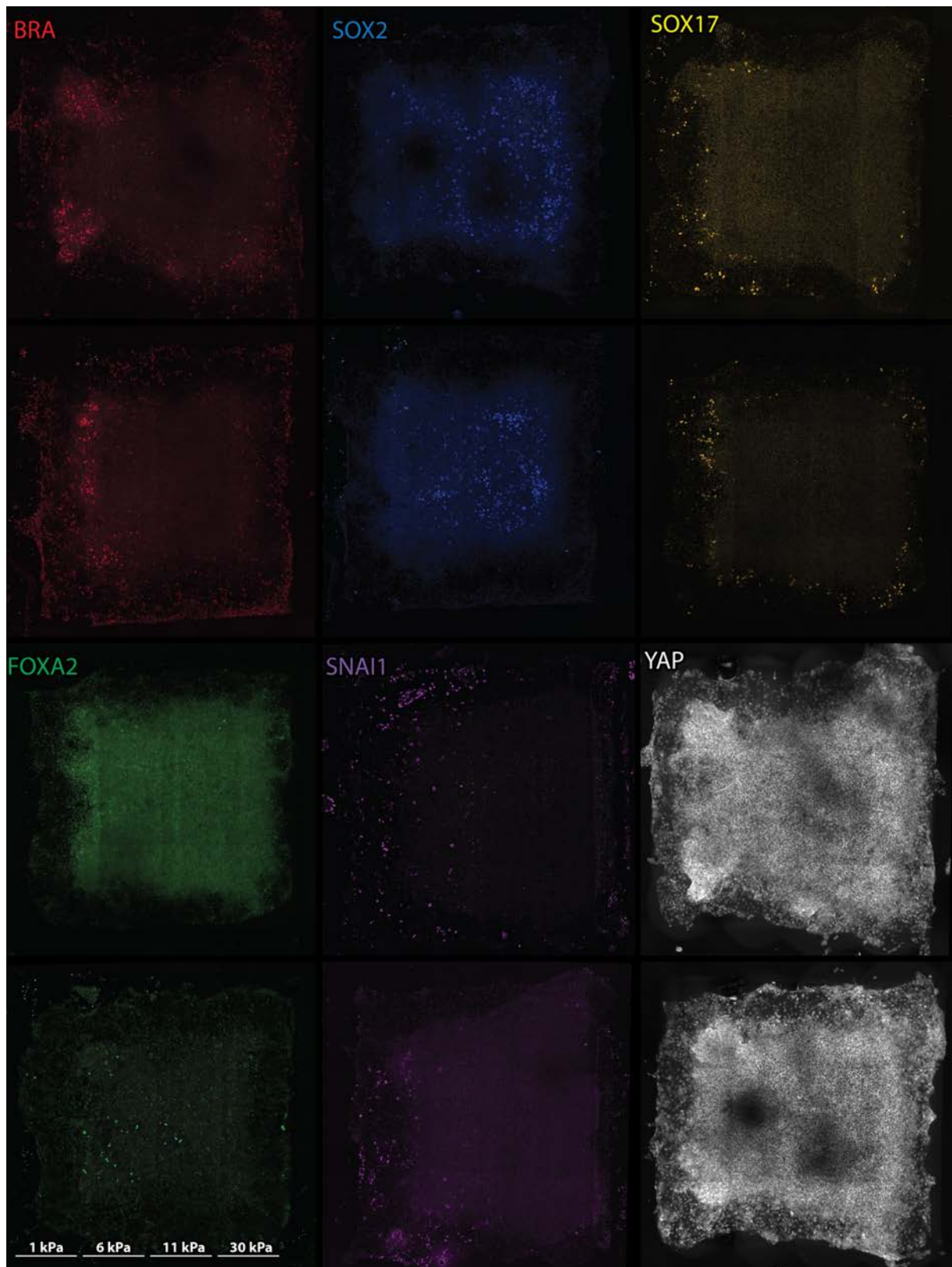


**Figure S19. High resolution images of representative mechano-structured niches at 72 h.** High magnification images of markers at 72 h, overlaid on gray nuclear stain. Niches are printed at 1000  $\mu$ m across. The color-coding has saturation correction applied to above images, with clipping and linear normalization to a 99.8% percentile bit-depth for improved visibility.

**Co-expression marker analysis in mechano-structured niches.** Co-staining was completed for the marker pairs: BRA:SOX2 and FOXA2:SOX17. Cells co-expressing the marker pairs were plotted. **Figure S20 a** shows marker expression pairs plotted in orthogonal directions beside representative images of dually stained micropatterns in **Figures S20 b and c**. Marker expression is shown as colored scatter-dots visible in **Figure S20 a, b**, showing how marker expression on a micropattern maps to the comparison shown in **Figure S20 a**. For colored dots, color is mapped according to co-expression of marker pairs displayed by each dot's angular position. **Figure S20 c**, shows the merged maximum intensity projection of makers with respective marker colors as per **Figure S20 a, b**.

According to the phenotypic characterization of BMP-induced micropatterned hiPSCs<sup>[27,28]</sup> (**Figure S21**), the molecular phenotype of micropatterned cells matches the cells of a Carnegie stage 7 human embryo<sup>[29]</sup>. SOX17+/FOXA2+ cells, which account for 19% of FOXA2 and/or SOX17 expressing cells, are reminiscent of the definite endoderm. SOX17+/FOXA2- cells, accounting for 23% of FOXA2 and/or SOX17 expressing cells, may be primordial germ-cell-like cells (hPGCLCs). SOX17-/FOXA2+ cells are reminiscent of gut endoderm, accounting for 58% of FOXA2 and/or SOX17-expressing cells. The identity of SOX17<sup>low</sup> cells and FOXA2<sup>low</sup> are not known.

BRA+/SOX2+ double-positive cells are found at the intersection between micropatterned regions with high expression of BRA and SOX2. As per the datasets in **Figures S21**, these cells are most likely to be reminiscent of an epiblast-like or primitive streak-like phenotype.

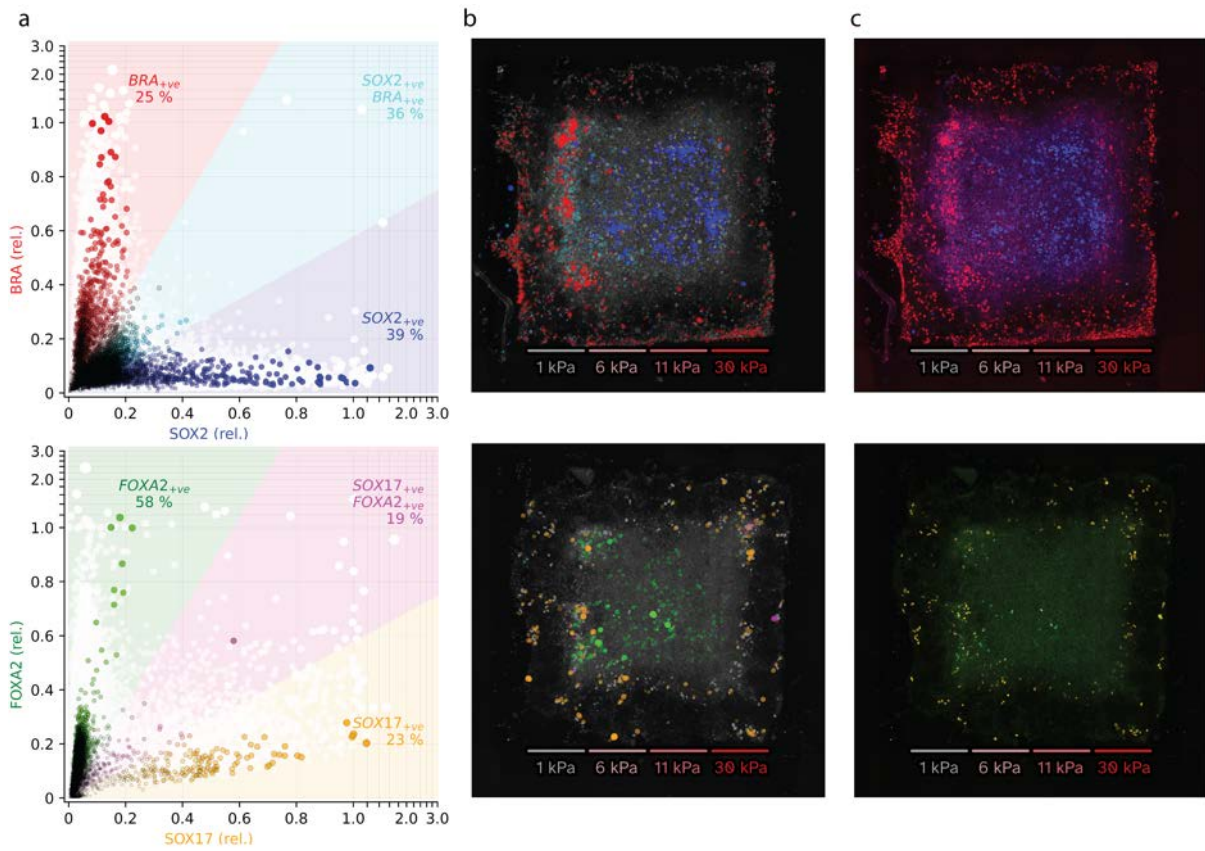
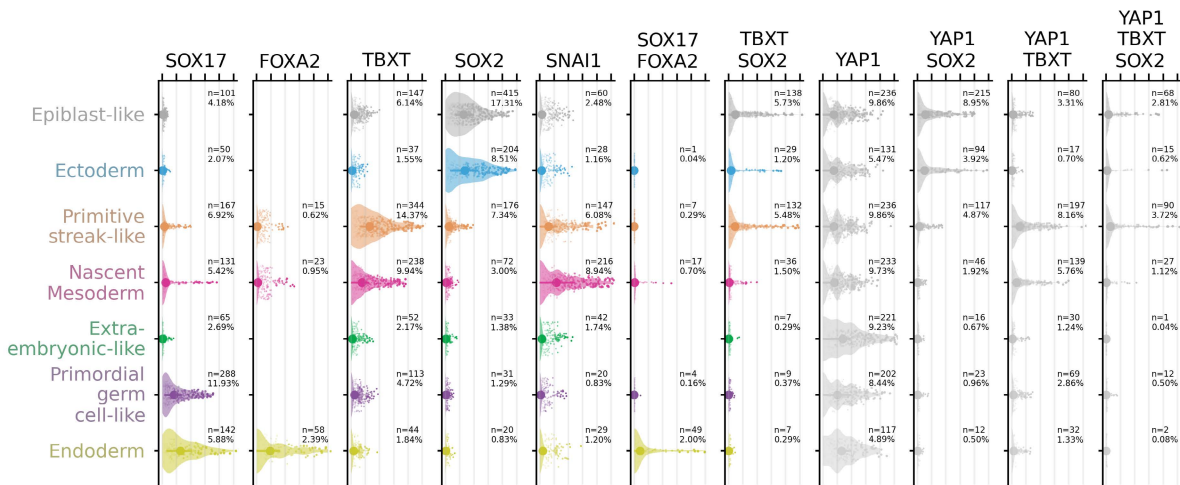


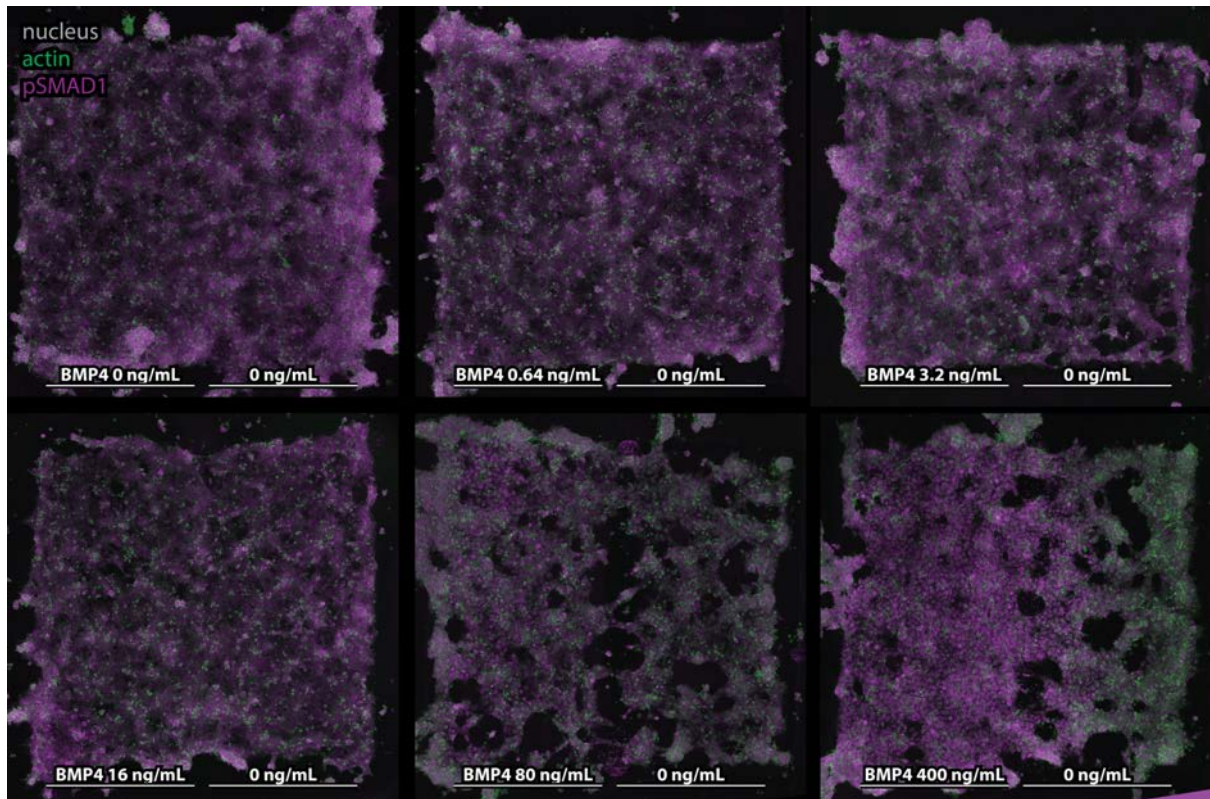
**Figure S20. Molecular analysis of cells expressing FOXA2:SOX17 and BRA:SOX2 in mechano-structured niches.** **a**, Marker intensity plots of cells displaying marker expression, with each dot representing intensity in a cell nucleus. Marker expression for markers is normalized by the average maximum intensity compared to all replicates. Color dots are mapped by angular position, with a relative expression greater than 0.1. White dots show all data while colored dots represent the nuclei that are shown in matching color in the images of **b** and **c**. **b** shows a merged grayscale maximum intensity projection of markers overlaid with the colored dots shown in **a**. **c**, shows the merged maximum intensity projection of markers with respective color as in **a**.



490

495

**Figure S21. scRNASeq data of cells grown in circular control niche (Minn et al., 2020) showing the cell types that match the expression of markers tested in the present study.**



500 **Figure S22. High magnification images of pSMAD1 expressing cells in morphogen-structured niches at 2 h.** Niches are printed at 1000  $\mu\text{m}$  across. pSMAD1 (purple), actin (green), nuclear stain (grey). Saturation correction applied to images, with clipping and linear normalization to a 99.8% percentile bit-depth for improved visibility.

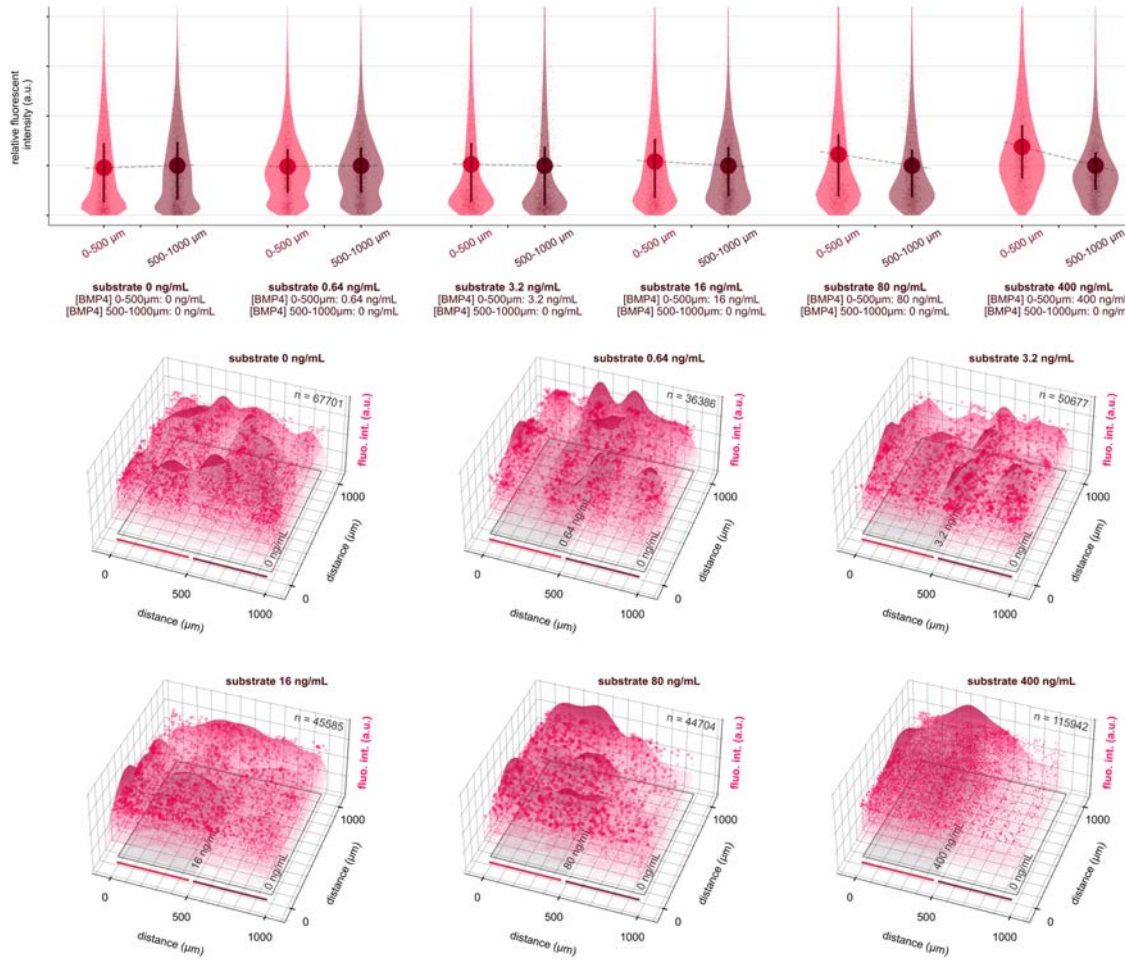
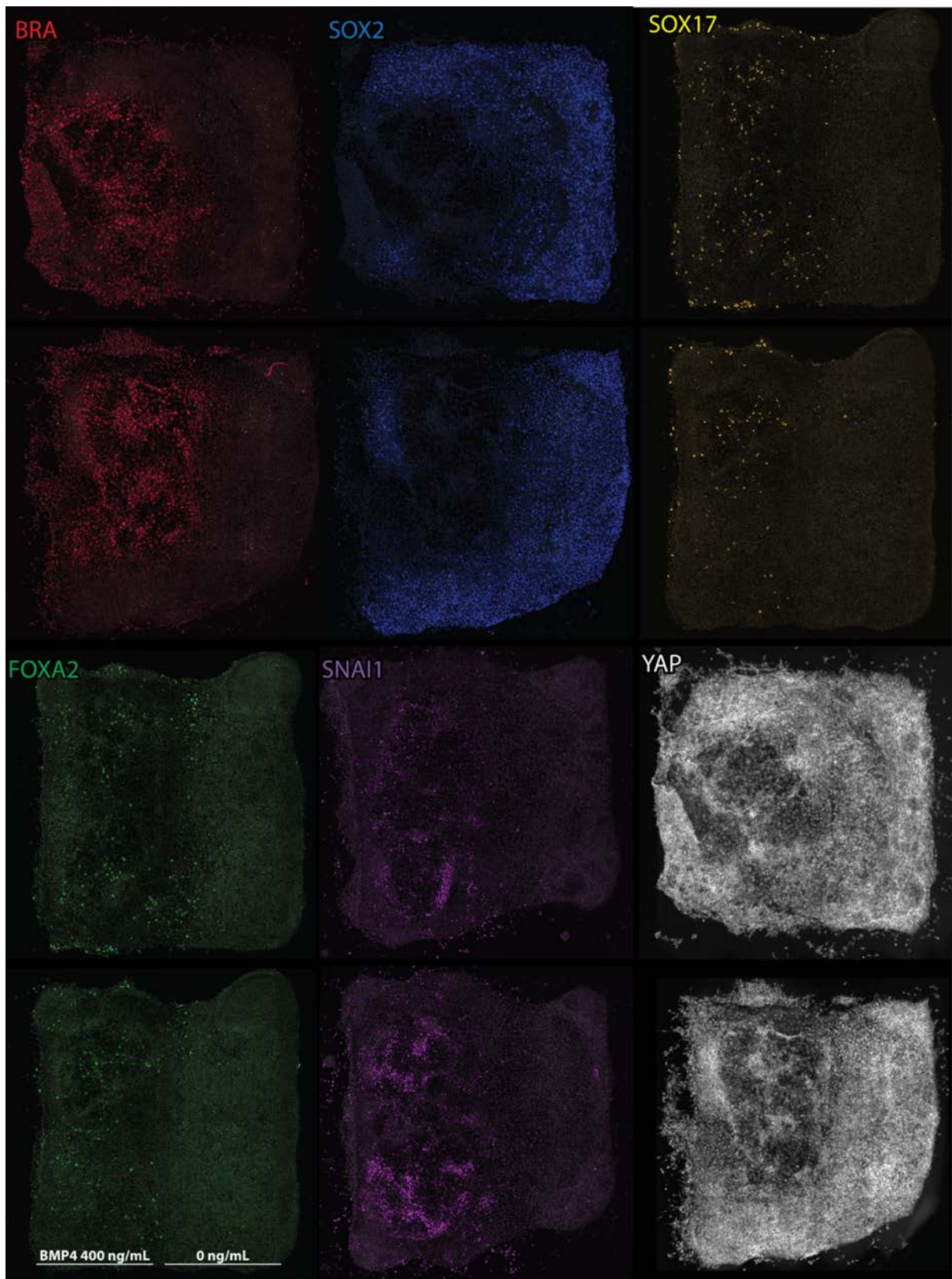


**Figure S23. Comparison of pSMAD1 N:C ratio associated with microstructure with three concentrations of BMP4.**

505

Violin plots compare the mean and distribution differences of pSMAD1 N:C ratio for different concentrations of BMP4 in the morphogen-structured niche at 2 h post-seeding, with normalization to the N:C ratio over the niche without BMP4. Substrate concentrations of BMP4 are shown for violin plot pairs (horizontal axis). 3D scatter, and surface plots are shown for replicate-pooled data, with labels of substrate BMP4 concentration, overlaid on the corresponding niche properties. A dose-dependent increase to the relative N:C ratio over regions with BMP4 was observed with increasing BMP4 concentration.



510 **Figure S24. Representative morphogen-structured niches at 72 h** showing high magnification images of marker expression  
at 72 h, overlaid on gray nuclear stain. Niches are printed at 1000  $\mu\text{m}$  across. Scale bar, 200  $\mu\text{m}$ . The color-coding has saturation  
correction applied to above images, with clipping and linear normalization to a 99.8% percentile bit-depth for improved  
visibility.

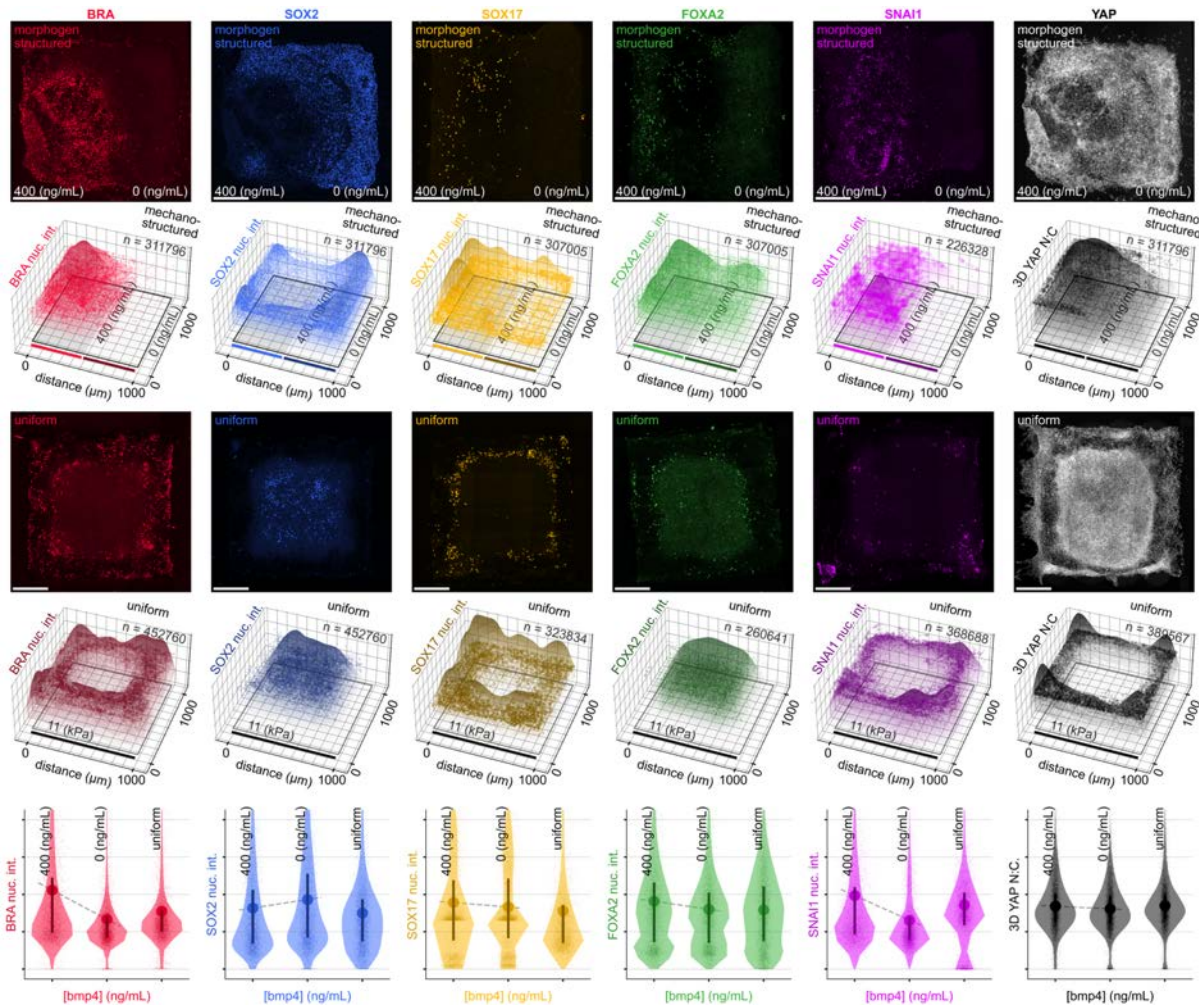


**Figure S25. Comparison of morphogen-structured and uniform niches at 72 h.** Rows 1 and 3 shows representative images

515 with overlaid text indicating the underlying niche type and niche orientation. The orientation of niches BMP4 containing region  
 with (left) and without BMP4 (right). Rows 2 and 4, show replicate data presented as 3D scatter and surface plots overlaid on a  
 representation of the corresponding niche. Row 5, Violin plots compare the mean and distribution, including mean and 1<sup>st</sup>/3<sup>rd</sup>  
 quartile lines of replicate data mapped to respective niche regions.

**Co-expression marker analysis in morphogen-structured niches.** As per Figure S26, the  
 520 co-expression of marker pairs SOX17:FOXA2 and BRA:SOX2 is presented. Double positive  
 SOX17+/FOXA2+ marked, which account for 26% of FOXA2 and SOX17 expressing cells,  
 may resemble expression patterns in cells of the definite endoderm. Similarly,  
 SOX17+/FOXA2- cells, accounting for 22% of FOXA2 and SOX17 expressing cells, may be  
 human primordial germ-cell-like cells (hPGCLCs). The identity of SOX17<sup>low</sup> cells and  
 525 FOXA2<sup>low</sup> is not known. SOX17-/FOXA2+ cells, accounting for 53% of FOXA2 and SOX17  
 expressing cells, are likely to resemble endoderm, or cells with low FOXA2 expression, may  
 resemble nascent mesoderm or primitive streak-like cells.

BRA+/SOX2+ double-positive cells are found at the intersection between micropatterned regions with high expression of BRA and SOX2. As per the datasets in **Figure S21**, these  
 530 cells are most likely to be reminiscent of an epiblast-like or primitive streak-like phenotype.

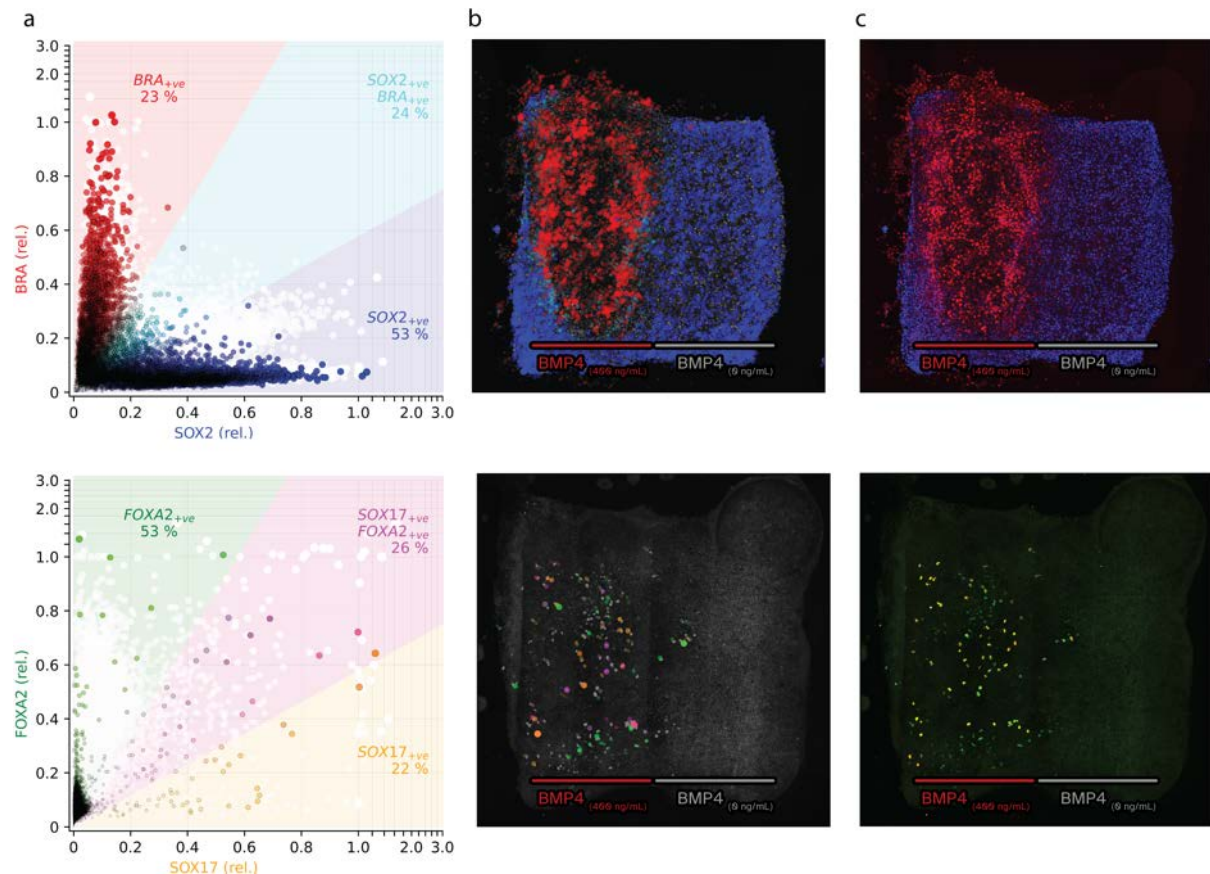
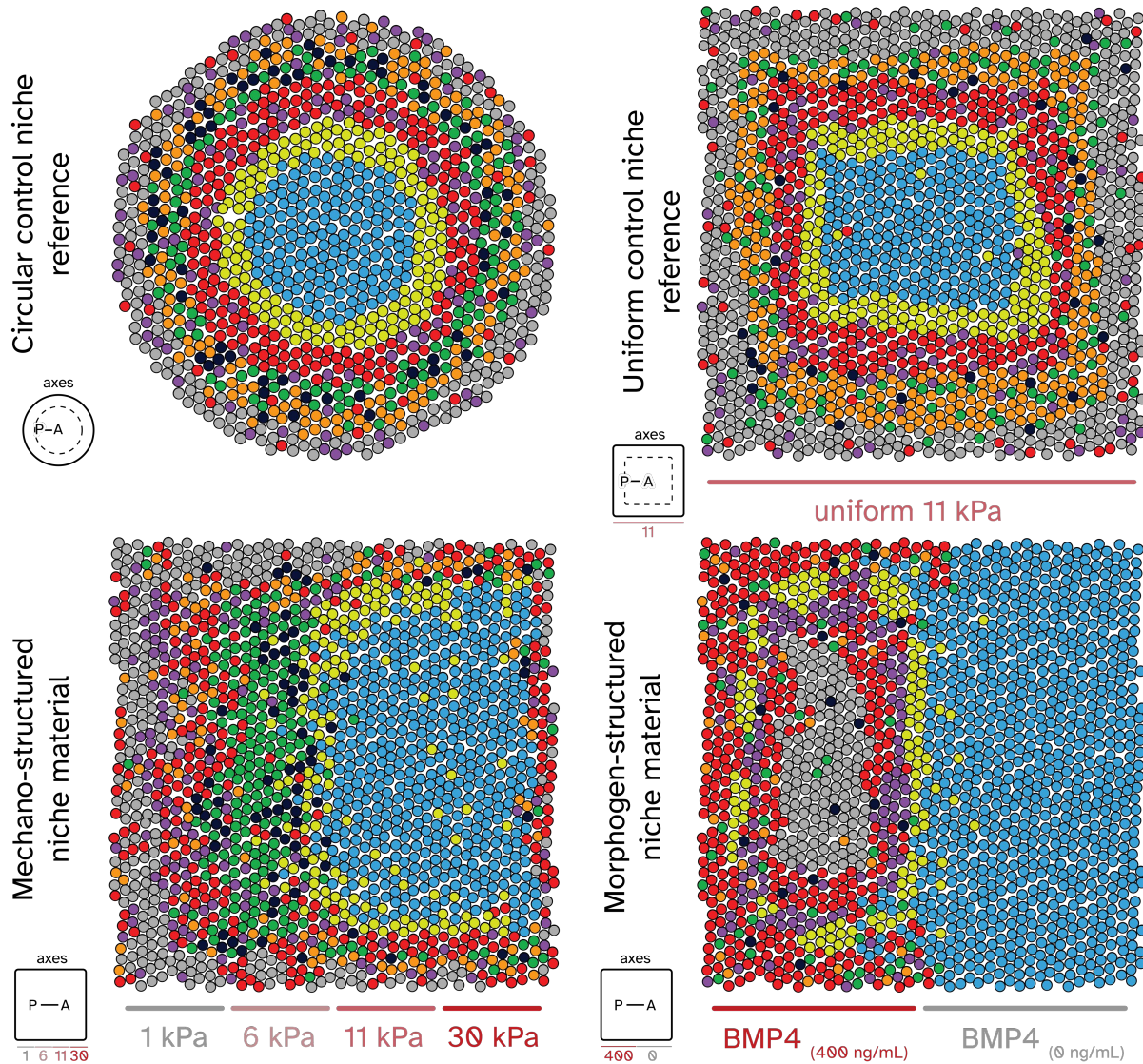


**Figure S26. Molecular analysis of cells expressing FOXA2:SOX17 and BRA:SOX2 in morphogen-structured niches .**  
**a**, Marker intensity plots of cells displaying marker expression, with each dot representing intensity in a cell nucleus. Marker expression for markers is normalized by the average maximum intensity compared to all replicates. Color dots are mapped by angular position, with a relative expression of greater than 0.1. White dots show all data while colored dots represent the nuclei that are shown in matching color in the images of **b** and **c**. **b**, shows a merged grayscale maximum intensity projection of markers overlaid with the colored dots shown in **a**. **c**, shows the merged maximum intensity projection of markers with respective color as in **a**.

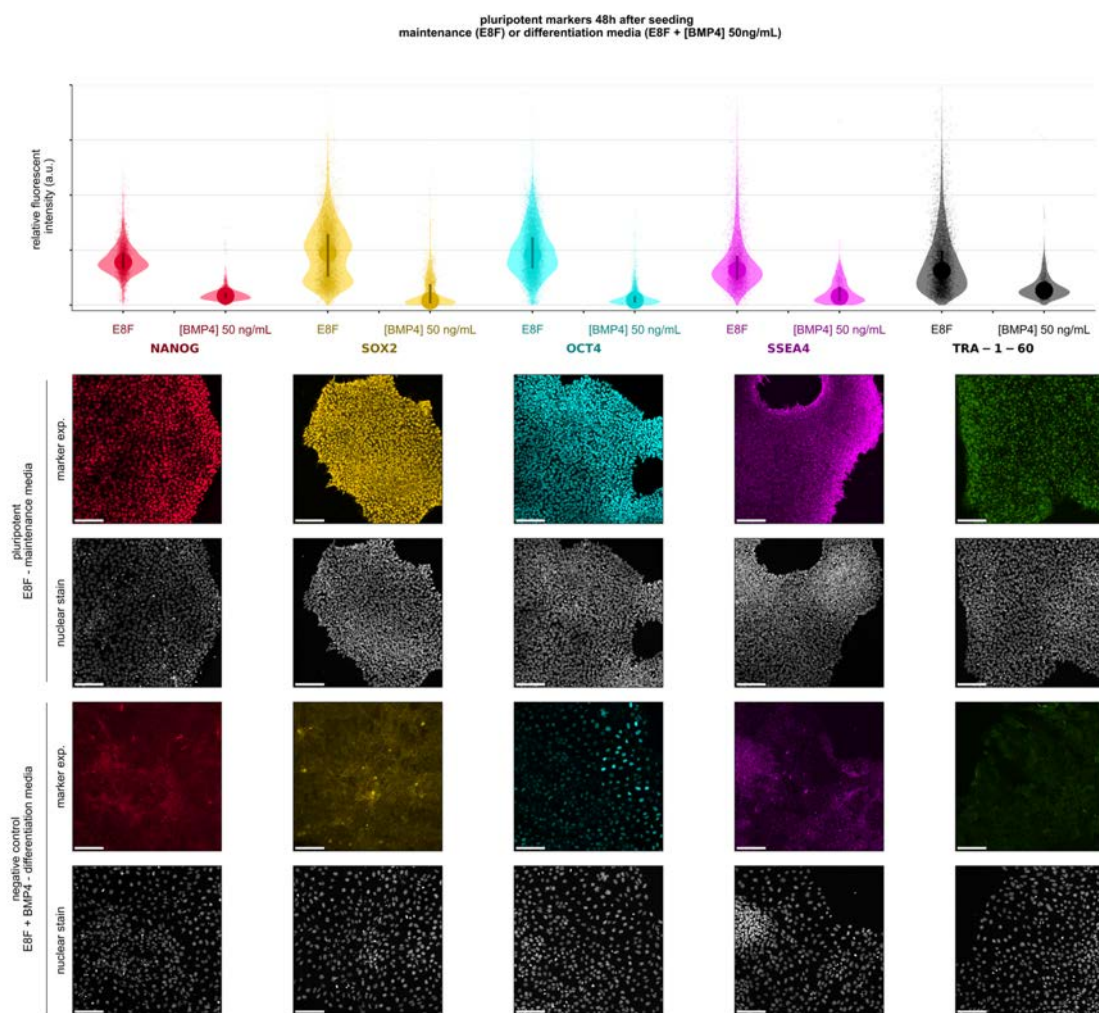
Summary of marker regionalization. We present a simplified plot showing the regionalization of the six markers, along with two co-expressed markers, as characterized in the present work (**Figure S27**). Through comparison with circular control micropatterns, and uniform niches, we highlight how microstructured mechano-chemical niche cues can be used to regionalize marker expression and enhance the organization and composition of engineered tissues, potentiating structures that better recapitulate their native counterparts.

● BRA ● BRA / SOX2 ● SNAIL ● YAP N:C<sup>high</sup> ● SOX17 ● FOXA2 ● SOX17 / FOXA2 ● SOX2



545

**Figure S27. A summary of marker regionalization across micropatterns.** A simplified plot showing the regionalization of the six markers, along with two co-expressed markers as characterized in the present work.



550

**Figure S28. Confirmation of hiPSC pluripotency as compared with differentiated negative control.** Shows quantification and representative images of pluripotent markers confirmed upon first receiving the HOIK1 cell line in passaged cell colonies comparing Essential 8 Flex (E8F) media or E8F media with BMP 4 (50 ng/mL).

**Table S 3. p-values table.** For null hypothesis testing, one-way ANOVA with Tukey post-hoc tests is used and listed throughout with p-values noted. In the below table we report p-values for all reported biological data – where  $p < 0.1$  is highlighted yellow, and  $p < 0.05$  is highlighted red.

**Figure 3**

| b) YAP v. RGD | 0 (mM)   | 0.03 (mM) | 0.13 (mM) | 0.5 (mM) | 2 (mM)   | c) YAP v. Young's Mod | 2.5 (kPa) | 5 (kPa)  | 10 (kPa) | 15 (kPa) |
|---------------|----------|-----------|-----------|----------|----------|-----------------------|-----------|----------|----------|----------|
| 0.03 (mM)     | 9.98E-01 |           |           |          |          | 5 (kPa)               | 9.20E-01  |          |          |          |
| 0.13 (mM)     |          | 1         | 9.99E-01  |          |          | 10 (kPa)              | 2.15E-02  | 1.91E-01 |          |          |
| 0.5 (mM)      |          | 1         | 1.00E+00  | 9.99E-01 |          | 15 (kPa)              | 2.60E-03  | 3.68E-02 | 9.27E-01 |          |
| 2 (mM)        | 7.38E-02 | 1.49E-01  | 6.87E-02  | 7.84E-02 |          | 20 (kPa)              | 3.50E-03  | 4.84E-02 | 9.62E-01 | 1        |
| 8 (mM)        | 7.50E-03 | 2.11E-02  | 5.90E-03  | 7.70E-03 | 5.80E-01 |                       |           |          |          |          |

**Figure 4**

| a) RUNX2 v. RGD         | 0 (mM)    | 0.03 (mM)   | 0.13 (mM) | 0.5 (mM)   | 2 (mM)      | b) AZR v. RGD         | 0 (mM)    | 0.03 (mM) | 0.13 (mM) | 0.5 (mM) | 2 (mM)   |
|-------------------------|-----------|-------------|-----------|------------|-------------|-----------------------|-----------|-----------|-----------|----------|----------|
| 0.03 (mM)               | 6.30E-01  |             |           |            |             | 0.03 (mM)             | 2.12E-01  |           |           |          |          |
| 0.13 (mM)               |           | 7.51E-01    | 9.99E-01  |            |             | 0.13 (mM)             | 3.00E-01  | 1.96E-01  |           |          |          |
| 0.5 (mM)                |           | 8.09E-01    | 1.00E+00  | 9.64E-01   |             | 0.5 (mM)              | 4.04E-02  | 1         | 2.79E-01  |          |          |
| 2 (mM)                  | 9.58E-02  | 2.11E-02    | 2.22E-01  | 2.41E-01   |             | 2 (mM)                | 4.81E-02  | 1.49E-01  | 1.82E-01  | 6.91E-01 |          |
| 8 (mM)                  | 5.07E-02  | 1.49E-01    | 1.19E-01  | 1.37E-01   | 4.95E-01    | 8 (mM)                | 2.50E-03  | 1.21E-01  | 1.17E-01  | 3.18E-01 | 6.43E-01 |
| c) RUNX2 v. Young's Mod | 2.5 (kPa) | 5 (kPa)     | 10 (kPa)  | 15 (kPa)   |             | d) AZR v. Young's Mod | 2.5 (kPa) | 5 (kPa)   | 10 (kPa)  | 15 (kPa) |          |
| 5 (kPa)                 | 9.50E-01  |             |           |            |             | 5 (kPa)               | 2.78E-01  |           |           |          |          |
| 10 (kPa)                |           | 9.86E-01    | 9.59E-01  |            |             | 10 (kPa)              | 0.00E+00  | 0.00E+00  |           |          |          |
| 15 (kPa)                |           | 6.39E-01    | 7.67E-01  | 6.72E-01   |             | 15 (kPa)              | 0.00E+00  | 4.00E-04  | 1.97E-01  |          |          |
| 20 (kPa)                | 1.36E-02  | 9.50E-03    | 5.20E-03  | 4.20E-03   |             | 20 (kPa)              | 0.00E+00  | 0.00E+00  | 1.60E-01  | 9.86E-01 |          |
| e) fat v. Young's Mod   | 2.5 (kPa) | 5 (kPa)     | 10 (kPa)  | 15 (kPa)   |             | f) fat v. RGD         | 0 (mM)    | 0.03 (mM) | 0.13 (mM) | 0.5 (mM) | 2 (mM)   |
| 5 (kPa)                 | 4.88E-02  |             |           |            |             | 0.03 (mM)             | 6.73E-01  |           |           |          |          |
| 10 (kPa)                | 9.20E-03  | 9.98E-02    |           |            |             | 0.13 (mM)             | 8.62E-01  | 5.20E-01  |           |          |          |
| 15 (kPa)                | 3.60E-03  | 1.40E-01    | 7.81E-01  |            |             | 0.5 (mM)              | 8.46E-01  | 1         | 9.80E-01  |          |          |
| 20 (kPa)                | 3.50E-03  | 4.10E-02    | 4.88E-01  | 4.41E-01   |             | 2 (mM)                | 1.03E-01  | 1.49E-01  | 9.40E-02  | 1.27E-01 |          |
| g) AZR v. BMP2          | 0 (ng/mL) | 1.6 (ng/mL) | 8 (ng/mL) | 40 (ng/mL) | 200 (ng/mL) | 8 (mM)                | 1.53E-01  | 2.30E-01  | 1.16E-01  | 1.08E-01 | 1.67E-02 |
| 1.6 (ng/mL)             | 7.15E-01  |             |           |            |             |                       |           |           |           |          |          |
| 8 (ng/mL)               |           | 8.91E-01    | 8.14E-01  |            |             |                       |           |           |           |          |          |
| 40 (ng/mL)              |           | 2.60E-01    | 9.07E-01  | 3.18E-01   |             |                       |           |           |           |          |          |
| 200 (ng/mL)             |           | 1.72E-01    | 1.49E-01  | 2.23E-01   | 9.61E-01    |                       |           |           |           |          |          |
| 1,000 (ng/mL)           |           | 3.90E-01    | 2.11E-01  | 4.75E-01   | 6.84E-01    |                       |           |           |           |          |          |

**Fig 5 m**

| BRA              | 1 kPa    | 6 kPa    | 11 kPa   | 30 kPa   | SNAIL1           | 1 kPa    | 6 kPa    | 11 kPa   | 30 kPa   |
|------------------|----------|----------|----------|----------|------------------|----------|----------|----------|----------|
| 6 kPa            | 0.00E+00 |          |          |          | 6 kPa            | 0.00E+00 |          |          |          |
| 11 kPa           | 0.00E+00 | 0.00E+00 |          |          | 11 kPa           | 0.00E+00 | 0.00E+00 |          |          |
| 30 kPa           | 0.00E+00 | 0.00E+00 | 0.00E+00 |          | 30 kPa           | 0.00E+00 | 0.00E+00 | 0.00E+00 |          |
| uniform (11 kPa) | 0.00E+00 | 0.00E+00 | 0.00E+00 | 0.00E+00 | uniform (11 kPa) | 1.11E-16 | 2.00E-13 | 0.00E+00 | 0.00E+00 |
| YAP              | 1 kPa    | 6 kPa    | 11 kPa   | 30 kPa   | SOX17            | 1 kPa    | 6 kPa    | 11 kPa   | 30 kPa   |



Fig 6



## References

- [1] J. S. Miller, K. R. Stevens, M. T. Yang, B. M. Baker, D.-H. T. Nguyen, D. M. Cohen, E. Toro, A. A. Chen, P. A. Galie, X. Yu, *Nat. Mater.* **2012**, *11*, 768.
- 565 [2] T. Xu, W. Zhao, J.-M. Zhu, M. Z. Albanna, J. J. Yoo, A. Atala, *Biomaterials* **2013**, *34*, 130.
- [3] L. Hockaday, K. Kang, N. Colangelo, P. Cheung, B. Duan, E. Malone, J. Wu, L. Girardi, L. Bonassar, H. Lipson, *Biofabrication* **2012**, *4*, 035005.
- 570 [4] D. B. Kolesky, K. A. Homan, M. A. Skylar-Scott, J. A. Lewis, *Proc. Natl. Acad. Sci.* **2016**, *113*, 3179.
- [5] H.-W. Kang, S. J. Lee, I. K. Ko, C. Kengla, J. J. Yoo, A. Atala, *Nat. Biotechnol.* **2016**, *34*, 312.
- [6] T. J. Ober, D. Foresti, J. A. Lewis, *Proc. Natl. Acad. Sci.* **2015**, *112*, 12293.
- [7] M. A. Skylar-Scott, J. Mueller, C. W. Visser, J. A. Lewis, *Nature* **2019**, *575*, 330.
- 575 [8] J. A. Brassard, M. Nikolaev, T. Hübscher, M. Hofer, M. P. Lutolf, *Nat. Mater.* **2020**, DOI 10.1038/s41563-020-00803-5.
- [9] A. Lee, A. R. Hudson, D. J. Shiwerski, J. W. Tashman, T. J. Hinton, S. Yerneni, J. M. Bliley, P. G. Campbell, A. W. Feinberg, *Science* **2019**, *365*, 482.
- 580 [10] D. B. Kolesky, R. L. Truby, A. S. Gladman, T. A. Busbee, K. A. Homan, J. A. Lewis, *Adv. Mater.* **2014**, *26*, 3124.
- [11] B. Richter, V. Hahn, S. Bertels, T. K. Claus, M. Wegener, G. Delaittre, C. Barner-Kowollik, M. Bastmeyer, *Adv. Mater.* **2017**, *29*, 1604342.
- [12] X. Ma, X. Qu, W. Zhu, Y.-S. Li, S. Yuan, H. Zhang, J. Liu, P. Wang, C. S. E. Lai, F. Zanella, *Proc. Natl. Acad. Sci.* **2016**, *113*, 2206.
- 585 [13] K. T. Lawlor, J. M. Vanslambrouck, J. W. Higgins, A. Chambon, K. Bishard, D. Arndt, P. X. Er, S. B. Wilson, S. E. Howden, K. S. Tan, *Nat. Mater.* **2020**, *1*.
- [14] P. Müller, R. Müller, L. Hammer, C. Barner-Kowollik, M. Wegener, E. Blasco, *Chem. Mater.* **2019**, *31*, 1966.
- [15] C. S. Chen, M. Mrksich, S. Huang, G. M. Whitesides, D. E. Ingber, *Science* **1997**, *276*, 1425.
- 590 [16] K. A. Mosiewicz, L. Kolb, A. J. Van Der Vlies, M. M. Martino, P. S. Lienemann, J. A. Hubbell, M. Ehrbar, M. P. Lutolf, *Nat. Mater.* **2013**, *12*, 1072.
- [17] Y. Luo, M. S. Shoichet, *Nat. Mater.* **2004**, *3*, 249.
- [18] J. A. Shadish, G. M. Benuska, C. A. DeForest, *Nat. Mater.* **2019**, *18*, 1005.
- 595 [19] H. Yin, Y. Ding, Y. Zhai, W. Tan, X. Yin, *Nat. Commun.* **2018**, *9*, 1.
- [20] B. Grigoryan, S. J. Paulsen, D. C. Corbett, D. W. Sazer, C. L. Fortin, A. J. Zaita, P. T. Greenfield, N. J. Calafat, J. P. Gounley, A. H. Ta, *Science* **2019**, *364*, 458.
- [21] P. Weiss, *J. Polym. Sci. Polym. Lett. Ed.* **1981**, *19*, 519.

- [22] C. K. Chan, G. S. Gulati, R. Sinha, J. V. Tompkins, M. Lopez, A. C. Carter, R. C. Ransom, A. Reinisch, T. Wearda, M. Murphy, *Cell* **2018**, *175*, 43.
- [23] U. Schmidt, M. Weigert, C. Broaddus, G. Myers, Springer, **2018**, pp. 265–273.
- [24] M. Weigert, U. Schmidt, R. Haase, K. Sugawara, G. Myers, **2020**, pp. 3666–3673.
- [25] A. Warmflash, B. Sorre, F. Etoc, E. D. Siggia, A. H. Brivanlou, *Nat. Methods* **2014**, *11*, 847.
- 605 [26] Y. Chen, C. A. Tristan, L. Chen, V. M. Jovanovic, C. Malley, P.-H. Chu, S. Ryu, T. Deng, P. Ormanoglu, D. Tao, *Nat. Methods* **2021**, *18*, 528.
- [27] K. T. Minn, Y. C. Fu, S. He, S. Dietmann, S. C. George, M. A. Anastasio, S. A. Morris, L. Solnica-Krezel, *eLife* **2020**, *9*, e59445.
- 610 [28] K. T. Minn, S. Dietmann, S. E. Waye, S. A. Morris, L. Solnica-Krezel, *Stem Cell Rep.* **2021**, *16*, 1210.
- [29] R. C. V. Tyser, E. Mahammadov, S. Nakanoh, L. Vallier, A. Scialdone, S. Srinivas, *Nature* **2021**, *600*, 285.
- 615 [30] S. Bergmann, C. A. Penfold, E. Slatery, D. Siriwardena, C. Drummer, S. Clark, S. E. Strawbridge, K. Kishimoto, A. Vickers, M. Tewary, T. N. Kohler, F. Hollfelder, W. Reik, E. Sasaki, R. Behr, T. E. Boroviak, *Nature* **2022**, *609*, 136.